MODELING MOMENTUM DISTRIBUTIONS OF POSITRON ANNIHILATION RADIATION IN SOLIDS

Ilja Makkonen

Laboratory of Physics
Helsinki University of Technology
Espoo, Finland

Dissertation for the degree of Doctor of Science in Technology to be presented with due permission of the Department of Engineering Physics and Mathematics, Helsinki University of Technology for public examination and debate in Auditorium E at Helsinki University of Technology (Espoo, Finland) on the 21st of September, 2007, at 13 o'clock.

Dissertations of Laboratory of Physics, Helsinki University of Technology
ISSN 1455-1802

Dissertation 150 (2007):
Ilja Makkonen: Modeling momentum distributions of positron annihilation radiation in solids

Opponent:
Prof. Mojmir Šob, Masaryk University, Brno, Czech Republic

Pre-examiners:
Dr. Bernardo Barbiellini, Northeastern University, Boston, USA
Dr. Stephan Eijt, Delft University of Technology, Netherlands

ISBN 978-951-22-8919-6 (print)
ISBN 978-951-22-8920-2 (electronic)
URL: http://lib.tkk.fi/Diss/2007/isbn9789512289202

MULTIPRINT OY / OTAMEDIA
ESPOO 2007

ABSTRACT OF DOCTORAL DISSERTATION	HELSINKI UNIVERSITY OF TECHNOLOGY P. O. BOX 1000, FI-02015 TKK http://www.tkk.fi

Author Ilja Makkonen

Name of the dissertation

Modeling momentum distributions of positron annihilation radiation in solids

Manuscript submitted 15th May 2007	Manuscript revised 15th August 2007
Date of the defence 21st September 2007 at 13 o'clock, main building of HUT, Otakaari 1, lecture hall E	
☐ Monograph	☒ Article dissertation (summary + original articles)

Department	Department of Engineering Physics and Mathematics
Laboratory	Laboratory of Physics
Field of research	Computational materials physics
Opponent(s)	Prof. Mojmir Šob, Masaryk University, Brno, Czech Republic
Supervisor	Prof. Martti Puska
Instructor	Prof. Martti Puska

Abstract

Positron annihilation spectroscopy is a materials characterization method especially applicable for studying vacancy defects in solids. In typical crystal lattices positrons get trapped at vacancy-type defects. By measuring positron lifetimes and momentum distributions of positron annihilation radiation one obtains information about the open volumes and the chemical environments of the defects.

Computational tools can be used in the analysis of positron annihilation experiments. Calculated lifetimes and momentum distributions of annihilating electron-positron pairs can be directly compared with experiment. Momentum spectra calculated for model defects can be used to determine, for example, characteristic effects of impurity atoms around vacancies. This information can be used when identifying the microscopic defect structures behind the measured spectra.

In this thesis momentum distributions of annihilating electron-positron pairs are calculated using quantum-mechanical electronic-structure methods based on the so-called density-functional theory. A numerical implementation is created based on the so-called projector augmented-wave method which enables the construction of accurate valence electron wave functions for the calculation of momentum densities. When studying positrons localized at vacancy defects their ionic structures are determined taking into account also the forces on ions due to the localized positron. First the computational scheme is validated by comparing computational results with ones measured by Compton scattering and positron annihilation spectroscopies for well-characterized samples (defect-free samples annealed at high temperatures, electron-irradiated samples containing vacancies).

The new methods are applied to the analysis of experimental positron data and resulting chemical identification of defects in different kinds of materials. Elemental (Si) and compound (GaN) semiconductors as well as metals and alloys (Al and Al-based alloys) are studied. An approach for quantitative chemical analysis of Al-based is justified using computations and the methods are also used to study the energetics of positron trapping in various solids and to show that the positron-induced lattice relaxations have an important role in the trapping process.

Keywords positron annihilation, electron momentum spectroscopies, density-functional theory

ISBN (printed) 978-951-22-8919-6	ISSN (printed) 1455-1802
ISBN (pdf) 978-951-22-8920-2	ISSN (pdf)
Language English	Number of pages 103

Publisher Laboratory of Physics, Helsinki University of Technology

Print distribution

☒ The dissertation can be read at http://lib.tkk.fi/Diss/2007/isbn9789512289202

VÄITÖSKIRJAN TIIVISTELMÄ	TEKNILLINEN KORKEAKOULU PL 1000, 02015 TKK http://www.tkk.fi

Tekijä Ilja Makkonen

Väitöskirjan nimi

Positroniannihilaatiosäteilyn liikemääräjakaumat kiinteissä aineissa: elektronirakenneohjelmiin perustuva mallinnus

Käsikirjoituksen päivämäärä 15.5.2007	Korjatun käsikirjoituksen päivämäärä 15.8.2007
Väitöstilaisuuden ajankohta 21.9.2007 klo 13, Teknillisen korkeakoulun päärakennus, Otakaari 1, sali E	
☐ Monografia	☒ Yhdistelmäväitöskirja (yhteenveto + erillisartikkelit)

Osasto	Teknillisen fysiikan ja matematiikan osasto
Laboratorio	Fysiikan laboratorio
Tutkimusala	Laskennallinen materiaalifysiikka
Vastaväittäjä(t)	Prof. Mojmir Šob, Masaryk University, Brno, Tšekin tasavalta
Työn valvoja	Prof. Martti Puska
Työn ohjaaja	Prof. Martti Puska

Tiivistelmä

Positroniannihilaatiospektroskopia on materiaalien karakterisointimenetelmä, joka soveltuu erityisesti kiinteiden aineiden kidevirheiden tutkimukseen. Kidehilassa positroni loukkuuntuu vakanssityyppisiin virheisiin. Mittaamalla positronin elinaikoja ja annihilaatiosäteilyn liikemääräjakaumia saadaan tietoa hilavirheiden avoimista tilavuuksista ja kemiallisista ympäristöistä.

Laskennalliset menetelmät ovat hyödyllisiä positroniannihilaatiokoetulosten analyysissä. Laskennallisia positronin elinaikoja ja annihiloituvien elektroni-positroniparien liikemääräjakaumia voidaan suoraan verrata kokeellisiin spektreihin. Mallirakenteille laskettujen liikemääräjakaumien avulla voidaan mm. selvittää vakanssia ympäröivien epäpuhtausatomeiden luonteenomainen signaali. Tätä tietoa voidaan käyttää mitatun signaalin aiheuttaneiden hilavirheiden mikroskooppisen rakenteen selvittämiseen.

Tässä väitöskirjassa annihiloituvien elektroni-positroniparien liikemääräjakaumia mallinnetaan kvanttimekaniikkaan ja ns. tiheysfunktionaaliteoriaan perustuvien elektronirakennelaskumenetelmien avulla. Uusi numeerinen toteutus perustuu ns. projector augmented-wave -menetelmään, joka mahdollistaa tarkkojen valenssielektroniaaltofunktioiden muodostamisen liikemääräjakaumien laskemista varten. Tutkittaessa vakanssivirheisiin loukkuuntuneita positronitiloja virheiden ionirakenne määritetään ottaen huomioon myös positronin lähinaapuri-ioneihin kohdistamat voimat. Mallinnusmenetelmän käyttökelpoisuus osoitetaan vertaamalla laskettuja tuloksia Compton-sirontakokeiden ja positroniannihilaatiomittausten tulosten kanssa hyvin karakterisoiduissa tapauksissa (virheettömät korkeassa lämpötilassa käsitellyt näytteet, vakansseja sisältävät elektronisäteilytetyt näytteet).

Uutta laskentamenetelmää sovelletaan työssä useisiin eri materiaaleihin, erityisesti kokeellisen positronidatan analyysiin ja vakanssivirheiden kemialliseen tunnistukseen. Tutkitaan puolijohteita kuten Si ja GaN sekä metalleja ja erityisesti Al-pohjaisia metalliseoksia. Laskuja käyttäen myös osoitetaan mm. metalliseosten kemialliseen analyysiin käytetyn menetelmän käyttökelpoisuus, tutkitaan positronin loukkuuntumisen energetiikkaa eri materiaaleissa ja osoitetaan positronin aiheuttamien hilarelaksaatioiden olevan olennainen osa positronin loukkuuntumisprosessia.

Asiasanat positroniannihilaatio, elektronin liikemääräspektroskopiat, tiheysfunktionaaliteoria

ISBN (painettu) 978-951-22-8919-6	ISSN (painettu) 1455-1802
ISBN (pdf) 978-951-22-8920-2	ISSN (pdf)
Kieli englanti	Sivumäärä 103

Julkaisija Fysiikan laboratorio, Teknillinen korkeakoulu

Painetun väitöskirjan jakelu

☒ Luettavissa verkossa osoitteessa http://lib.tkk.fi/Diss/2007/isbn9789512289202

Preface

This thesis has been prepared in the Computational Nanoscience group, COMP, led by Academy Prof. Risto Nieminen at the Laboratory of Physics of the Helsinki University of Technology, during the years 2004–2007.

I am especially grateful to my instructor Prof. Martti Puska for his contribution and expertise in positron physics, electronic structure calculations and other topics related to my thesis. During the early part of the thesis work I had the pleasure of working with late Prof. Kimmo Saarinen. He and his students at the experimental positron group at the Laboratory of Physics provided us with vast amounts of experimental data and interesting problems from the field of semiconductor physics. The work on metals and alloys with Prof. Alfredo Dupasquier, Dr. Paola Folegati and Dr. Rafael Ferragut from the Como positron group of the Politecnico di Milano became another integral part of the thesis work. The collaboration with Dr. Mikko O. Hakala from the University of Helsinki enabled us to broaden the set of possible applications of our methods also to Compton scattering. I want also to thank the present and former members of the Laboratory of Physics for the past years.

Financial support from the Academy of Finland, National Graduate School in Materials Physics, and the Viljo, Yrjö and Kalle Väisälä Foundation and computer resources from the Center of Scientific Computing are also acknowlegedged.

Friends, family and Terhi, Thank you!

Espoo, May 2007

Ilja Makkonen

Contents

List of publications

This thesis consists of an overview and the following publications:

I I. Makkonen, M. Hakala, and M. J. Puska, *Calculation of valence electron momentum densities using the projector augmented-wave method*, J. Phys. Chem. Solids **66**, 1128–1135 (2005).

II I. Makkonen, M. Hakala, and M. J. Puska, *Modeling the momentum distributions of annihilating electron-positron pairs in solids*, Phys. Rev. B **73**, 035103:1–12 (2006).

III M. Rummukainen, I. Makkonen, V. Ranki, M. J. Puska, K. Saarinen, and H.-J. L. Gossmann, *Vacancy-Impurity Complexes in Highly Sb-Doped Si Grown by Molecular Beam Epitaxy*, Phys. Rev. Lett. **94**, 165501:1–4 (2005).

IV S. Hautakangas, I. Makkonen, V. Ranki, M. J. Puska, K. Saarinen, X. Xu, and D. C. Look, *Direct evidence of impurity decoration of Ga vacancies in GaN from positron annihilation spectroscopy*, Phys. Rev. B **73**, 193301:1–4 (2006).

V A. Calloni, A. Dupasquier, R. Ferragut, P. Folegati, M. M. Iglesias, I. Makkonen, and M. J. Puska, *Positron localization effects on the Doppler broadening of the annihilation line: Aluminum as a case study*, Phys. Rev. B **72**, 054112:1–6 (2005).

VI P. Folegati, I. Makkonen, R. Ferragut, and M. J. Puska, *Analysis of electron-positron momentum spectra of metallic alloys as supported by first-principles calculations*, Phys. Rev. B **75**, 054201:1–10 (2007).

VII I. Makkonen and M. J. Puska, *Energetics of positron states trapped at vacancies in solids*, Phys. Rev. B **76**, 054119:1–10 (2007).

The author has had an active role in all the phases of the research reported in this thesis. He has developed key parts of the computer codes used in all of the publications and participated in the planning of the calculations and the interpretation of results of both experiments and computations. The author has performed all calculations in Publications I–IV and VII and the calculations presented in Publications V and VI have been done under his guidance. He has written the first drafts of publications I, II and VII completely and partly those of Publications IV and VI.

1 Introduction

Point defects can affect or even determine many macroscopic properties of crystalline solids even though their size is only of the order of a few atoms and even if their concentrations are only of the order of ppm. For example, in metals and alloys vacancies mediate diffusion and thereby directly affect their mechanical properties. In semiconductor materials atomic defects are electically active and consequently affect the electrical and optical properties of the material. The open volume at vacancy defects enables one to probe them using positrons because the repulsion of the positive nuclei is reduced at vacancies enabling effective positron trapping. By measuring the positron annihilation radiation which gives information on the positron lifetime in the sample and carries the net momentum of the annihilating electron-positron pairs, one gains information on the electronic structure of defects in the sample [1, 2]. Positron annihilation spectroscopy has been widely used in the research of defects in materials which is also its application in this thesis. Another important application of positrons in the studies of solids materials has since the beginning been the study of the topologies of Fermi surfaces of metals (for recent work see Refs. [3, 4]) and high-T_c superconductors [5, 6]. Recent progresses and future prospects in the studies of nanocrystals are reviewed in Ref. [7]. The experimental and theoretical basis of positron annihilation was developed in the 1960's and in the 1970's [8, 9]. The study of vacancy-defects began from vacancies in metals and then widened to semiconductors on a larger scale in the beginning of the 1980's.

Since the measured positron lifetime correlates with the magnitude of electronic density at the annihilation site positron lifetime measurements give information on the open volumes at the vacancy defects. The measured momentum distribution of annihilation radiation gives chemical information on the annihilation sites, for example, reveals impurity atoms next to vacancies. The momentum density of the annihilating electron-positron pairs is sometimes referred to as the electron momentum density "as seen by the positron" because the momentum of the positron is usually considerably smaller than that of the electron. Furthermore, a positron localized at a vacancy defect is a local probe of the electronic structure of the defect. The reduced overlap of the positron state with high-momentum core electrons compared to that in the perfect bulk can be seen in measurements. The chemical identification of defects is very much based on differences in core electron structures between the impurity atoms and the host lattice atoms. Thus, there are impurity-induced differences at high momenta in the mo-

mentum spectra.

Computational tools can be used in the analysis of the results of positron annihilation experiments [9]. One can create an atomic-scale model for a given defect and calculate from first principles the corresponding annihilation characteristics such as the positron lifetime and the momentum distribution of the annihilating electron-positron pairs. The results can then directly be compared with the experiment and the agreement in experimentally well-characterized cases validates the computational scheme. Then it can be used in the analysis of experimental results. In this thesis the focus is on the development of accurate and practical calculation methods for describing positron annihilation with valence electrons and especially for the description of momentum distributions of annihilating valence electron-positron pairs. In practice, a commonly used electronic-structure code and the so-called projector augmented-wave (PAW) method [10] are applied to these purposes. The PAW method is band-structure method that enables all-electron accuracy with the efficiency of the pseudopotential method. This is especially important when studying vacancy defects in semiconductors for which large supercells are needed. It also enables one to efficiently study first-row elements, transition metals and rare-earth elements. Furthermore, it does not suffer from transferability problems and enables a full-potential treatment. From the point of view of momentum density calculations the important aspect is that it enables the construction of all-electron wave functions that contain accurate information on the high momentum Fourier components.

The methods developed in the thesis are applied to the interpretation of positron annihilation experiments, predicting properties of defects and the behavior of positrons in solids, and trying to solve problems and test hypotheses which can not be approached using experiments only. The ultimate goal in the defect modeling has been treating the defects (their ionic and electronic structures) as well as the positron state at the vacancy fully on the first-principles basis, to obtain the annihilation characteristics with as few assumptions and artificial constraints as possible. The main interest in the thesis is on the modeling of the positron annihilation characteristics but also Compton profile (electron momentum density) calculations are made as a first step in the testing of the method.

There are two primary classes of crystalline materials to which the computational methods developed in the thesis are applied. First of all, semiconductors and, secondly, metals and metallic alloys, especially Al-based alloys. By applying the same methods to a variety of different materials we have

also gained a better understanding of the limitations of the computational methods.

Vacancies are important is semiconductors because they can have a role in doping and electrical compensation. Native vacancies have been observed at high concentrations in many compound semiconductors. Low-energy positron beams [8] can be used in defect studies of epitaxial layers and surface regions. Reviews of positron annihilation studies made for semiconductors can be found in Refs. [1, 2].

In metallic alloys solute-vacancy association is one of the basic processes controlling the precipitation phenomenon. Vacancies mediate transport of solute atoms and contribute to the stability of precipitates by reducing misfit stresses between them and the matrix material [11]. Precipitation is technologically important since it improves a number of light alloys used, for example, in the vehicle and aircraft industry. In addition to the vacancy solute association and kinetics of precipitation, processes such as age-hardening, severe plastic deformation, fatigue and fracture can be studied using positron annihilation. A review on the achievements of positron annihilation techniques in the study of light alloys can be found in Ref. [12].

Publications I and II of the thesis present our computational methods in the context of Compton profile calculations and the calculations of momentum distributions of annihilating electron-positron pairs, respectively. Publications III and IV deal with semiconductor materials and are for the most part based on experiments. In them our computations are used to analyze the measured data. The materials in Publications V and VI are Al and Al-based alloys, respectively, and the calculations are used to demonstrate the effects of positron localization on the measured Doppler broadening spectrum and to justify a method for chemical analysis of vacancy-solute association in alloys. Publication VII is an entirely computational study examining in more detail the energetics of the positron trapping process and the importance of positron-induced ionic relaxations.

This overview is organized as follows. Section 2 discusses the behavior of positrons in solids and describes the basic principles of the main experimental methods based on positron annihilation in the context of defect studies. Section 3 presents the basics of electronic structure theory, the modeling of positron annihilation characteristics and the actual implementation of the methods used in the thesis. Section 4 discusses the applications presented in the thesis in more detail, especially those in Publications III–VII. Finally, Sec. 5 summarizes and concludes the overview and the thesis.

2 Positrons in solids and positron annihilation spectroscopy

This section briefly describes the behavior of positrons in solids and the principles of positron annihilation experiments. More information can be found in Refs. [1, 2, 8, 9].

In positron annihilation experiments the positron source is typically a β^+-active ^{22}Na source. A 1.27 MeV photon is emitted simultaneously with the positron. In positron lifetime studies the detection of this gamma is used to signal the birth of a positron. In conventional lifetime studies fast (unmoderated) positrons having kinetic energies of the order of 1 MeV (for a ^{22}Na source $E_{\max} = 0.54$ MeV) are used. When entering the sample the positron very rapidly loses its kinetic energy. At high kinetic energies the dominating processes are ionization and core electron excitations. At lower energies the most important processes are electron-hole excitations. Phonon processes become important at around 1 eV. In semiconductors the electron energy band gap prevents electron-hole excitations with a smaller energy than the gap. The phonon processes, however, are so effective that the positron thermalization times in semiconductors are comparable to those in metals. The positron thermalization times are of the order of 1–3 ps only which is much less than typical positron lifetimes in solids (100–300 ps). The thermalization phase of the positrons can be modeled, for example, with Monte Carlo simulations or with the Boltzmann equation including annihilation and trapping terms [9]. In a wide-gap insulator a positron with kinetic energy less than the band gap can also lose energy in positronium (Ps) formation. The excitation of an electron from a valence band is possible because in the final state the Ps binding energy (6.8 eV in vacuum) is gained.

After the thermalization phase the positron momentum distribution has reached the time-independent form and its spatial distribution continues to evolve. Its behavior can be described using the so-called diffusion-annihilation equation [9] in which there are terms describing also the positron annihilation and trapping. In the band picture the thermalized positron is thought to be at the Γ ($\mathbf{k} = 0$) point at the bottom of the parabolic free-electron-like positron energy band. If there is even a small concentration (around 10^{16} cm^{-3} in the case of neutral defects in semiconductors [2]) of neutral or negatively charged vacancy-type defects in the sample the positron very effectively gets trapped at a vacancy defect because the Coulomb repulsion of the nuclei is lower at the vacancy. Figure 1 shows calculated positron densities of localized and delocalized positron states in

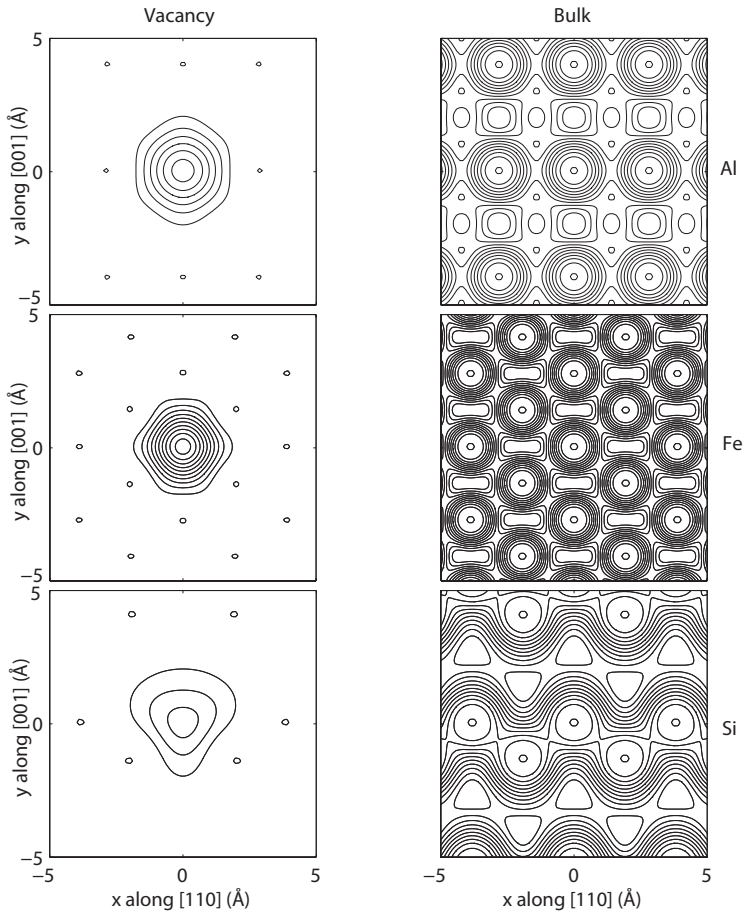

Figure 1: Positron densities in monovacancies (left, contour spacing 0.01 Å^{-3}) in Al, Fe and Si and in corresponding perfect lattices (right, contour spacing one tenth of the maximum value). The dots in the figures denote the locations of the nuclei on the figure plane. From Publication VII.

different materials. The process taking care of the energy and momentum transfer is in the case of metals electron-hole excitation. In semiconductors and insulators the positron binding energy to the defect can be smaller than the energy band gap. In this case electron-hole excitations from the valence band to the conduction band are not possible. The present picture is that the electron excitation from a localized defect state to the conduction band can account for the energy loss at vacancy-defects in semiconductors [13]. A mechanism that further increases the trapping rate in semiconductors is the fact that defects can have a net charge and negative defects trap positrons more effectively than neutral ones. Positive defects are not considered to trap positrons [13]. The positron can get trapped into weakly localized Rydberg states at negative defects [13]. This can be followed by a transition into a localized ground state via the electron-hole excitation process. The trapping models in the literature have always assumed a fixed defect geometry. The effect of the localized positron on the defect geometry and the energetics of positron trapping is analyzed in Publication VII of this thesis (see Sec. 4.6).

In positron annihilation experiments one obtains information on the sample and the defects it contains by measuring the photons emitted when positron annihilates with an electron. For a review on experimental methods utilizing positron annihilation see Ref. [1]. Typically, one monitors the two-gamma annihilation in which the mass of the electron-positron pair is transformed into energy in the form of two 511-keV γ-quanta. The positron lifetime can be measured as the time difference between the 1.27 MeV birth γ-quantum and the 511-keV annihilation γ. The measured lifetime spectra are sums of exponentially decaying components,

$$-\frac{dn(t)}{dt} = \sum_i I_i \lambda_i \exp(-\lambda_i t). \tag{1}$$

Above, $n(t)$ is the probability for the positron to be alive at time t. The spectrum is determined by the relative intensities, I_i, and the annihilation rates, λ_i, of different annihilation states. For a ground state at a vacancy the annihilation rate λ_i is the inverse of the corresponding lifetime component τ_i (assuming that there is no detrapping) whereas for the delocalized bulk state the measured λ_i is an effective quantity affected also by the positron trapping rate. The trapping in a homogeneous solid is described by kinetic equations [14] (a nice review including discussion on trapping models can be found in Ref. [15]). The lifetime components τ_i associated with vacancy defects are correlated with the open volume of the defect. At vacancies,

voids and dislocations (with kinks or jogs) the electron density is lowered compared to the value in the perfect bulk. This results in the lowering of the annihilation rate and increase in the corresponding lifetime component.

The differences in the electronic structures of the positron annihilation sites in the sample are reflected also in the momenta of the 511-keV annihilation photons which carry the net momenta of the annihilating electron-positron pairs. Measuring their momentum distribution enables one to gain chemical information on the annihilation sites in the sample. This can in practice be done by the so-called Doppler broadening spectroscopy in which the broadening of the 511-keV annihilation line is measured. The coincidence technique [16] in which the simultaneous detection of both annihilation gammas is required improves the peak-to-background ratio considerably and enables chemical analysis of vacancy defects on the basis of differing core-electron structures of impurity and host lattice atoms. The peak-to-background ratio can be further improved by measuring the energy of both annihilation gammas with two Ge detectors and requiring the energy conservation. This also improves the energy resolution of the setup by the factor of $\sqrt{2}$. Figure 2 shows an example of measured Doppler broadening spectra. Another way to measure the net momentum of the annihilating pair is to measure the angular correlation (deflection from the 180° angle) of the two γ-quanta using one- or two-dimensional detectors (1D- or 2D-ACAR; ACAR stands for Angular Correlation of Annihilation Radiation).

When studying defects in semiconductors one is often interested in near-surface regions. Fast positrons have so high kinetic energy that they, in practice, only probe the bulk of the material. Therefore, the positrons have to be moderated first and then accelerated to the kinetic energy corresponding to the desired mean stopping depth (usually the kinetic energy is between 0–40 keV). Due to the moderation process the birth gamma does not give the time when the positron enters the sample. Therefore, the conventional low-energy positron beams can only be used for Doppler broadening measurements. The problem can be circumvented by using pulsed positron beams in which the time the positron enters the sample is obtained from the pulsing electronics.

Most of the experiments in the publications of this thesis have been made with fast positrons (positron lifetime and coincidence Doppler broadening measurements). A conventional low-energy positron beam was used in Publication III.

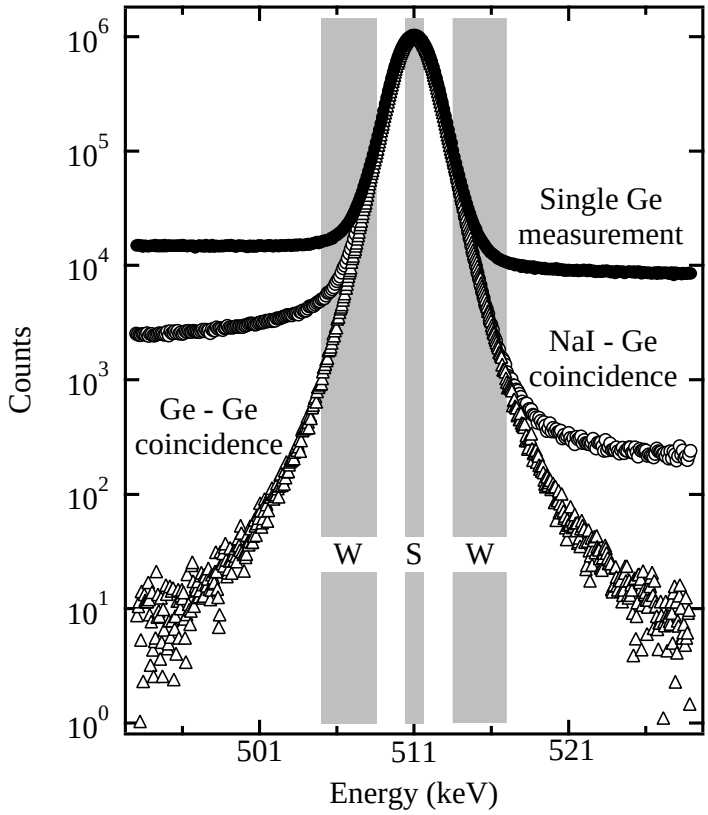

Figure 2: Doppler broadening spectra obtained in different data collection modes. The definition of the shape parameters S and W is shown. The data (from Refs. [17, 18]) has been measured in a bulk ZnO sample where no positron trapping at defects is observed at 300 K. Courtesy of Dr. F. Tuomisto.

3 Theory and models

3.1 Electronic-structure calculations and density-functional theory

This section deals with the methods used in electronic structure calculations of the thesis. A recent review on the basic electronic-structure theory can be found in the book by Martin [19]. All the equations shown are in Hartree atomic units ($\hbar = m_e = e = 4\pi/\epsilon_0 = 1$) so that, for example, the units of length and energy are 1 $a_0 = 0.529$ Å and 1 Ha = 27.2 eV, respectively.

The Hamiltonian of a system of interacting electrons at sites $\mathbf{r}_i$ and nuclei with charges Z_I and masses M_I at sites $\mathbf{R}_I$ can be written as

$$\begin{aligned} H(\mathbf{r}) = &-\frac{1}{2}\sum_i \nabla_i^2 - \sum_{i,I} \frac{Z_I}{|\mathbf{r}_i - \mathbf{R}_I|} + \frac{1}{2}\sum_{i\neq j} \frac{1}{|\mathbf{r}_i - \mathbf{r}_j|} \\ &- \sum_i \frac{1}{2M_I}\nabla_I^2 + \frac{1}{2}\sum_{I\neq J} \frac{Z_I Z_J}{|\mathbf{R}_I - \mathbf{R}_J|}. \end{aligned} \tag{2}$$

As the inverse masses of the nuclei, $1/M_I$, are very small one usually first assumes that the kinetic energy of the nuclei is zero and then later treats the degrees of freedom of the nuclei ($\mathbf{R}_I$) classically. This is the so-called Born-Oppenheimer (or adiabatic) approximation.

In all systems of any interest to solid-state physicists there are more than two electrons. In the case of the Hamiltonian of Eq. (2) the many-body Schrödinger equation is not separable and solving or even approximating is becomes a very difficult and impractical approach. The most practical approach in most cases is the density-functional theory (DFT), which is based on the theorem by Hohenberg and Kohn [20]. It states that a universal functional for the energy in terms of the electron density $n(\mathbf{r})$ can be defined, valid for any external potential $V_{\text{ext}}(\mathbf{r})$,

$$E_{\text{HK}}[n] = T[n] + E_{\text{int}}[n] + \int d\mathbf{r}\, V_{\text{ext}}(\mathbf{r}) n(\mathbf{r}) + E_{II}. \tag{3}$$

For any particular $V_{\text{ext}}(\mathbf{r})$, the exact ground-state energy of the system is the global minimum of this functional and the density $n(\mathbf{r})$ that minimizes the functional is the exact ground-state density. Above, $T[n]$ is the kinetic energy functional, $E_{\text{int}}[n]$ the interaction energy of electrons, and E_{II} is the interaction energy of the nuclei. In practice, the functional of Eq. (3) is unknown and it is not clear what would be the best way to minimize it. In

principle, there is a way to reformulate the functional and determine it but for this one also needs information on the lowest energy many-body wave function corresponding to a given electron density n [21, 22].

The ansatz suggested by Kohn and Sham [23] is based on an analogy between the true interacting many-body system and a noninteracting system with the same density n. The energy functional is written as

$$E_{\rm KS}[n] = T_s[n] + \frac{1}{2}\int d\mathbf{r}\, d\mathbf{r}' \frac{n(\mathbf{r})n(\mathbf{r}')}{|\mathbf{r}-\mathbf{r}'|} + \int d\mathbf{r}\, V_{\rm ext}(\mathbf{r})n(\mathbf{r}) + E_{II} + E_{\rm xc}[n], \quad (4)$$

where $T_s[n]$ is the kinetic energy of a system of noninteracting electrons with density n and $E_{\rm xc}[n]$ is the so-called exchange-correlation energy functional. By comparing Eqs. (3) and (4) one sees that $E_{\rm xc}[n]$ represents the difference in kinetic energies and internal interaction energies between the true interacting many-body system and the fictitious independent-particle system with the electron-electron interactions replaced by the Hartree energy,

$$E_{\rm xc}[n] = T[n] - T_s[n] + E_{\rm int}[n] - \frac{1}{2}\int d\mathbf{r}\, d\mathbf{r}' \frac{n(\mathbf{r})n(\mathbf{r}')}{|\mathbf{r}-\mathbf{r}'|}. \quad (5)$$

The exchange-correlation energy functional is unknown and thus has to be approximated.

With the analogy to the system of noninteracting electrons in the external potential $V_{\rm ext}(\mathbf{r})$ the minimization of the energy functional of Eq. (4) leads to the following set of single-particle equations which are solved in a self-consistent manner,

$$-\frac{1}{2}\nabla^2\psi_i(\mathbf{r}) + V_{\rm eff}(\mathbf{r})\psi_i(\mathbf{r}) = \varepsilon_i\psi_i(\mathbf{r}), \quad (6)$$

where the effective potential is written as

$$V_{\rm eff}(\mathbf{r}) = \int d\mathbf{r}' \frac{n(\mathbf{r}')}{|\mathbf{r}-\mathbf{r}'|} + V_{\rm ext}(\mathbf{r}) + \frac{\delta E_{\rm xc}[n]}{\delta n(\mathbf{r})}. \quad (7)$$

Above, the last term is called the exchange-correlation potential. The electron density is obtained by summing over occupied states,

$$n(\mathbf{r}) = \sum_{i=1}^{N} |\psi_i(\mathbf{r})|^2. \quad (8)$$

Equations (6)–(8) are termed the Kohn-Sham equations and they together with approximations for $E_{xc}[n]$ form the basis of practical electronic-structure calculations within DFT.

The most common approximation for the exchange-correlation energy is the local-density approximation [23] (LDA) in which the exchange-correlation energy density at point $\mathbf{r}$, $\varepsilon_{xc}(\mathbf{r})$, is assumed to be the same as the exchange-correlation energy per electron in a homogeneous electron gas with density $n(\mathbf{r})$,

$$E_{\rm xc}[n] = \int d\mathbf{r}\, \varepsilon_{\rm xc}^{\rm hom}(n(\mathbf{r}))n(\mathbf{r}). \tag{9}$$

Moreover, there are semi-local functionals which depend also on the gradient of the electron density. These are termed generalized-gradient approximations (GGA), and nonlocal orbital-dependent functionals such as so-called hybrid functionals in which part of the exchange energy is replaced by the Hartree-Fock exchange (for reviews see Refs. [24, 19]). However, only the LDA is used in this thesis. We use the LDA parametrization by Perdew and Zunger [25] based on the quantum Monte Carlo calculations by Ceperley and Alder [26].

3.2 Positron state and annihilation calculations

The first detailed theoretical studies on positron annihilation in a homogeneous interacting electron gas taking into account electron-positron correlations were performed by Kahana [27] and by Carbotte and Kahana [28] in the 1960's. In the case of homogeneous systems it is natural to operate in momentum space and define a momentum-dependent enhancement factor as $\gamma(p) = \rho(p)/\rho^0(p)$, where $\rho^0(p)$ is the non-interacting electron gas momentum density and $\rho(p)$ is that at the positron's site in the interacting system. The enhancement factor describes the increase in the positron annihilation probability due to many-body interactions (screening of the positron by electrons). Kahana and coworkers found that as one approaches the Fermi momentum the annihilation probability increases. Above the Fermi momentum the momentum density is effectively zero in contrast to the case of homogeneous interacting electron gas that has a high-momentum tail above the Fermi momentum [29]. The lifetimes predicted by the many-body theories are substantially shorter than the ones expected according to the noninteracting Sommerfeld model due to increased annihilation rate and thus they are in much better agreement with the experiment.

Later, Salvadori and Carbotte [30] studied the enhancement in the case of tightly bound core electrons. The total enhancement was found substantial but less than that for free electrons and the momentum-dependence is weak suggesting that the independent-particle model prediction (see below)

works for core electrons.

The case of periodic solids was studied by Hede and Carbotte [31] using a nearly-free-electron model. The periodic potential introduces high-momentum (Umklapp) components to wave functions. Their enhancement factor was found to be approximately constant and somewhat lower than for the central free-electron parabola.

The many-body calculations behind the approximations used in this thesis for describing the electron-positron correlation effects are the ones by Arponen and Pajanne [32] and Lantto [33]. The background of the practical methods used in this thesis for solving the positron state and annihilation characteristics is, however, elsewhere. The computational methods applied are based on the extension of the DFT for a many-electron system to the case of finite electron and positron densities. The extension is called the two-component DFT [34]. In a density-functional approach it is natural to use as far as possible instead of the electron and positron wave functions the corresponding densities and write the enhancement factors as functionals of the real-space densities instead of as a function of the momentum. In the DFT there is no simple connection between the real-space electronic charge density and the electron momentum density [35] and although the Kohn-Sham single-particle wave functions are used in practice in momentum density calculations they have no well-defined physical meaning. The electron-positron correlation energy functionals and enhancement factors appearing in the two-component DFT are parametrized with the help of many-body calculations made for homogeneous electron-positron plasmas with varying electron and positron densities. Most practical calculations done for realistic solids and defects in solids in the past 20 years are in practice based on the two-component DFT or most often on some simplification of it as in the case of the present thesis.

In the so-called two-component density-functional theory [34] the usual DFT is generalized to the case in which there are two density components of mutually distinguishable particles, namely the electron density n_- and the positron density n_+. The Kohn-Sham ansatz is in this case written as

$$E[n_-, n_+] = F[n_-] + F[n_+] - \frac{1}{2}\int d\mathbf{r}\, d\mathbf{r}' \frac{n_-(\mathbf{r})n_+(\mathbf{r}')}{|\mathbf{r}-\mathbf{r}'|} + \int d\mathbf{r}\, V_{\text{ext}}(\mathbf{r})[n_-(\mathbf{r}) - n_+(\mathbf{r})] + E_{II} + E_{\text{c}}^{\text{e-p}}[n_-, n_+] \quad (10)$$

where $F[n]$ is the familiar single-component functional

$$F[n] = T_s[n] + \frac{1}{2}\int d\mathbf{r}\, d\mathbf{r}' \frac{n(\mathbf{r})n(\mathbf{r}')}{|\mathbf{r}-\mathbf{r}'|} + E_{\rm xc}[n], \tag{11}$$

and $E_{\rm c}^{\rm e-p}[n_-, n_+]$ is the so-called electron-positron correlation energy functional taking into account electron-positron correlations beyond the electron-positron Hartree term. Minimization of the energy functional of Eq. (10) leads to the following set of modified Kohn-Sham equations for electrons and positrons, respectively,

$$-\frac{1}{2}\nabla^2\psi_i(\mathbf{r}) + \left[\frac{\delta E_{\rm xc}[n_-]}{\delta n_-(\mathbf{r})} - \phi(\mathbf{r}) + \frac{\delta E_{\rm c}^{\rm e-p}[n_+,n_-]}{\delta n_-(\mathbf{r})}\right]\psi_i(\mathbf{r}) = \varepsilon_i\psi_i(\mathbf{r}), \tag{12}$$

$$-\frac{1}{2}\nabla^2\psi_i^+(\mathbf{r}) + \left[\frac{\delta E_{\rm xc}[n_+]}{\delta n_+(\mathbf{r})} + \phi(\mathbf{r}) + \frac{\delta E_{\rm c}^{\rm e-p}[n_+,n_-]}{\delta n_+(\mathbf{r})}\right]\psi_i^+(\mathbf{r}) = \varepsilon_i^+\psi_i^+(\mathbf{r}), \tag{13}$$

where the sum of the total Hartree potential and the external potential due to nuclei is written as

$$\phi(\mathbf{r}) = \int d\mathbf{r}'\, \frac{-n_-(\mathbf{r}') + n_+(\mathbf{r}')}{|\mathbf{r}-\mathbf{r}'|} - V_{\rm ext}(\mathbf{r}). \tag{14}$$

The density components are obtained by summing over occupied Kohn-Sham orbitals,

$$n_-(\mathbf{r}) = \sum_{i=1}^{N_-} |\psi_i(\mathbf{r})|^2, \qquad n_+(\mathbf{r}) = \sum_{i=1}^{N_+} |\psi_i^+(\mathbf{r})|^2, \tag{15}$$

where N_- and N_+ are the numbers of electrons and positrons in the system, respectively.

In practice the electron-positron correlation energy is evaluated within the LDA and the parametrizations are based on many-body calculations of homogeneous electron-positron plasmas with varying electron and positron densities. Only the zero-positron-density limit is well known. Still, some fully self-consistent two-component DFT studies for positrons localized at vacancies have been made [36, 37, 38, 39, 40]. In this thesis we use a simpler scheme (sometimes called the "conventional scheme") in which we make the following approximations even if we are modeling a localized positron state. First of all, the positron does not affect the average electron density $n_-(\mathbf{r})$. (The positron and its screening electron cloud are considered to form a neutral quasiparticle.) Secondly, the positron state and annihilation characteristics are calculated at the zero-positron density limit of the

two-component DFT. The effects of these two approximations are shown to largely cancel each other and the approach produces results that agree with self-consistent calculations made within the Boroński-Nieminen two-component formalism [37]. In practice, our calculations are done as follows: first the electronic structure is calculated without the effect of the positron. Then the positron state is solved in potential

$$V_+(\mathbf{r}) = \phi'(\mathbf{r}) + V_{\mathrm{corr}}(\mathbf{r}), \tag{16}$$

where the Hartree potential $\phi'(\mathbf{r})$ is now due to electrons and nuclei only and $V_{\mathrm{corr}}(n_-(\mathbf{r}))$ is the zero-positron-density limit of the electron-positron correlation potential $\delta E_{\mathrm{c}}^{\mathrm{e-p}}[n_-, n_+]/\delta n_+(\mathbf{r})$. We are interested in the case of only one positron in the lattice. In Eq. (16) the self-interaction correction is made; i.e., the self-direct Hartree potential of the positron is canceled by the self-exchange-correlation potential.

Publications II, VI and VII of this thesis include calculations in which the ionic structures of vacancy defects are optimized taking into account also the forces on ions due to the localized positron. In our approach the energy of the system comprising one positron and a lattice can be written as a sum of the positron energy eigenvalue and the energy of the defect supercell (electron-ion system). The force on ions due to the localized positron can be calculated using the Hellman-Feynman theorem when the positron Hamiltonian and the positron state are known. The force on ion j reads

$$\begin{aligned}\mathbf{F}_j^+ &= -\nabla_j \varepsilon_+ = -\nabla_j \langle\psi^+|H(\mathbf{r})|\psi^+\rangle \\ &= -\langle\psi^+|\nabla_j H(\mathbf{r})|\psi^+\rangle - \varepsilon_+ \nabla_j \underbrace{\langle\psi^+|\psi^+\rangle}_{\equiv 1} = -\langle\psi^+|\nabla_j H(\mathbf{r})|\psi^+\rangle, \end{aligned} \tag{17}$$

where the gradient is taken with respect to $\mathbf{R}_j$, the coordinates of the ion j. For the Hamiltonian $H(\mathbf{r})$ we use an approximate expression of the so-called atomic superposition method [9, 41] in which the positron annihilation characteristics are calculated using superimposed charge densities and potentials of free atoms,

$$H(\mathbf{r}) = -\frac{1}{2}\nabla^2 + V_+(\mathbf{r}), \tag{18}$$

where

$$V_+(\mathbf{r}) = \sum_j V_{\mathrm{Coul}}^{\mathrm{at},j}(|\mathbf{r} - \mathbf{R}_j|) + V_{\mathrm{corr}}\Big(\sum_j n_-^{\mathrm{at},j}(|\mathbf{r} - \mathbf{R}_j|)\Big). \tag{19}$$

Above, $V_{\mathrm{Coul}}^{\mathrm{at},j}(\mathbf{r})$ and $n_-^{\mathrm{at},j}(\mathbf{r})$ are the Coulomb potential and the charge density of the free atom j, respectively. The force calculations are discussed further in Publication II. One must note that within the conventional scheme

one has to approximately take into account also the position-dependence of valence electron states because if the total energy functional is written in the practical way as a sum of Kohn-Sham eigenvalues minus double counting corrections there are no such double counting corrections for the electron-positron interactions as there are for the electron-electron interactions. Therefore, in contrast to the plain electronic-structure calculations there is no such error cancellation in the force calculation which enables one to limit the summation only to the core electron states (see Refs. [42, 43]).

Once the ionic and electronic structure and the positron state are solved one is ready to calculate the positron annihilation characteristics such as the positron lifetime τ which is the inverse of the positron annihilation rate λ, [34]

$$\lambda = \frac{1}{\tau} = \pi r_e^2 c \int d\mathbf{r}\, n_+(\mathbf{r}) n_-(\mathbf{r}) g(0; n_+; n_-), \tag{20}$$

where r_e is the classical radius of electron and c the speed of light. In principle, the annihilation rate is proportional to the overlap of electron and positron densities but as in the DFT the densities $n_-(\mathbf{r})$ and $n_+(\mathbf{r})$ are only average ones and do not take into account the local pileup of electron density at the positron, the pair-correlation function of electron-positron densities, $g(0; n_+; n_-)$, evaluated at the positron (also called the "contact density") is included in Eq. (20). In practice, also Eq. (20) is evaluated using the LDA and the contact density is derived from many-body calculations for homogeneous electron-positron plasmas. As we use in our calculations the zero-positron-density limits of functionals, Eq. (20) is written in the form

$$\lambda = \pi r_e^2 c \int d\mathbf{r}\, n_+(\mathbf{r}) n_-(\mathbf{r}) \gamma(n_-(\mathbf{r})), \tag{21}$$

where $\gamma(n_-(\mathbf{r})) = g(0; n_+ = 0; n_-)$ is termed the enhancement factor and is the zero-positron-density limit of g. The calculation of momentum densities of annihilating electron-positron pairs is discussed later in this Section.

In practice we use for the correlation potential $V_{\mathrm{corr}}(n_-)$ and enhancement factor $\gamma(n_-)$ the parametrizations by Boroński and Nieminen [34]. Their zero-positron-density parametrizations for the electron-positron correlation energy are consistent with the calculations by Arponen and Pajanne [32] and the Boroński-Nieminen enhancement factor is parametrized according to the calculations by Lantto [33]. The use of these functionals implies assuming a metallic screening. Still, we use them also for semiconductors. There are semi-empiric models taking into account dielectric properties of the solid [44] but we prefer not to use them because of their semi-empiric nature.

What also has to be noted here is that there exists also a GGA parametrization for the enhancement factor and correlation potential [45, 46]. In Publication II we have tested using the state-dependent enhancement scheme (see below) its applicability to momentum density calculations and compared its results to results calculated with the Boroński-Nieminen LDA. The GGA describes in general better the intensity of Doppler spectra at high momenta than the Boroński-Nieminen LDA. However, in the case of ratio spectra it fails in some cases. Furthermore, the GGA parametrization involves one semi-empiric parameter. For these reasons we prefer to use the Boroński-Nieminen LDA.

The main drawback of the LDA enhancement factor is that it overestimates annihilation with core and d-electrons. Instead of comparing the absolute values of lifetimes with experiment we compare in the case of vacancy defects the increase in the lifetime compared to the value in bulk. In the case of momentum distributions we use a ratio representation (see below) in which the overestimated intensity at high momenta is canceled. A systematic study in which positron lifetimes are calculated for most of the elements of the Periodic Table using different enhancement factors can be found in Ref. [47].

The momentum density of electrons is written in the independent-particle model (IPM) as [48]

$$\rho(\mathbf{p}) = \frac{1}{(2\pi)^3} \sum_j \left| \int d\mathbf{r} \exp(-i\mathbf{p}\cdot\mathbf{r})\psi_j(\mathbf{r}) \right|^2, \tag{22}$$

where the summation goes over occupied single-particle states. Equation (22) is based on the Hartree-Fock theory but it is conventionally used within the DFT as well [49]. Within the DFT the electron momentum density (EMD) $\rho(\mathbf{p})$ of Eq. (22) is not, as opposed to the charge density $n(\mathbf{r})$, exact even if the exchange and correlation functionals were exact. In the DFT the correlation effects beyond the independent-particle model are usually modeled by the so-called Lam-Platzman (LP) correlation correction [50] which is isotropic within the LDA. In this thesis the LP correction is not used for simplicity and because it does not affect the anisotropy plots we have used in Publication I. In order to get an anisotropic correlation correction one has to go beyond the DFT and LDA.

The quantity measured in Compton scattering experiments, the Compton profile $J(p_z)$, is related to the EMD via

$$J(p_z) = \int\int dp_x\, dp_y\, \rho(\mathbf{p}), \tag{23}$$

where the one integrates over the planes perpendicular to the scattering vector. The above equation is based on the impulse approximation [51] which is valid if the energies transferred in scattering processes are much larger than the binding energies of the electronic states involved.

For annihilating electron-positron pairs the independent-particle model [the counterpart of Eq. (22)] reads [52]

$$\rho(\mathbf{p}) = \pi r_e^2 c \sum_j \left| \int d\mathbf{r} \exp(-i\mathbf{p}\cdot\mathbf{r}) \psi_+(\mathbf{r}) \psi_j(\mathbf{r}) \right|^2, \tag{24}$$

where r_e is the classical radius of electron and c the speed of light. The independent-particle model lacks the short-range electron-positron correlations that increase the annihilation rate compared to one calculated using the average electron and positron densities $n_-(\mathbf{r})$ and $n_+(\mathbf{r})$ only [$\gamma \equiv 1$ in Eq. (21)]. To overcome this, several models utilizing the enhancement factor such as the one in Eq. (21) have been developed in the past. The first requirement the models have to fulfill is that the momentum density of the annihilating electron-positron pairs is consistent with the positron annihilation rate λ, i.e.,

$$\lambda = \int d\mathbf{p}\, \rho(\mathbf{p}). \tag{25}$$

The most commonly used model in practical calculations is what we call the state-independent LDA scheme [53, 54]

$$\rho(\mathbf{p}) = \pi r_e^2 c \sum_j \left| \int d\mathbf{r} \exp(-i\mathbf{p}\cdot\mathbf{r}) \psi_+(\mathbf{r}) \psi_j(\mathbf{r}) \sqrt{\gamma(n_-(\mathbf{r}))} \right|^2, \tag{26}$$

in which a position-dependent enhancement factor is introduced in the IPM expression. In practice we use the square root of the enhancement factor for the densities, $\sqrt{\gamma(n_-(\mathbf{r}))}$, in the spirit of Eq. (21). The screening cloud is in a sense averaged over the electronic states j. There are also similar models in which the enhancement factor is not only position- but also **k**- (a Kahana-type momentum dependence) and possibly state-dependent meaning that the enhancement factor describes the distortion of individual electron-positron wave functions (see, for example, Ref. [55] and references therein). For d-electron transition metals with non-parabolic bands the enhancement is often written in terms of the energy instead of the momentum [56, 57, 58] by equating $p/p_F = \sqrt{E_{j\mathbf{k}}/E_F}$, where $E_{j\mathbf{k}}$ is the one-particle energy of an electron in the jth band at Bloch vector **k** measured from the bottom of the conduction band, p_F and E_F are the Fermi momentum and

Fermi energy, respectively, and $p = |\mathbf{k}| \leq p_F$. A recent review on various electron-positron interaction theories can be found in Ref. [59].

Another model which is the one primarily used in this thesis is the so-called state-dependent scheme [60]

$$\rho(\mathbf{p}) = \pi r_e^2 c \sum_j \gamma_j \left| \int d\mathbf{r} \exp(-i\mathbf{p}\cdot\mathbf{r}) \psi_+(\mathbf{r}) \psi_j(\mathbf{r}) \right|^2 . \tag{27}$$

Above, $\gamma_j = \lambda_j^{\mathrm{LDA}}/\lambda_j^{\mathrm{IPM}}$, where

$$\lambda_j^{\mathrm{LDA}} = \pi r_e^2 c \int d\mathbf{r}\, n_+(\mathbf{r}) n_j(\mathbf{r}) \gamma(n_-(\mathbf{r})) \tag{28}$$

is the annihilation rate of state j within the LDA or GGA and λ_j^{IPM} is the corresponding IPM ($\gamma \equiv 1$) annihilation rate. Above, $n_j(\mathbf{r})$ is the density corresponding to electron state j. In the state-dependent model the momentum dependence of term j in the sum is the same as in the IPM and for a homogeneous system there is no Kahana-type momentum dependence [61]. The energy dependence of the state-dependent enhancement factors in the case of Cu is discussed in Ref. [61]. One possible way to view Eq. (27) is to think it as a sum of *normalized* IPM momentum densities weighted with respective partial annihilation rates λ_j^{LDA}.

The two models [Eqs. (26) and (27)] mentioned above are critically benchmarked in Publication II using experimental Doppler spectra measured for well-annealed bulk samples as references. We have used two kinds of representations. We either (*i*) plot the absolute value of the Doppler spectrum (either using linear or logarithmic scale) or (*ii*) we plot the spectra as a ratio to a reference spectrum (typically bulk Al). In the latter case the systematic errors in the theoretical (and those possibly in experimental spectra) are for the most part canceled. When comparing the results with the experiment we make the following two observations.

1. The absolute intensities of Doppler spectra at high momenta are overestimated in the state-dependent model whereas the intensities are well reproduced in the state-independent LDA scheme. Especially strong the overestimation is in the case of materials with d electrons. However, the state-independent LDA results oscillate about the experimental spectrum whereas the behavior of the spectra calculated using the state-dependent scheme is very similar to that of the experimental one (see also Ref. [60]).

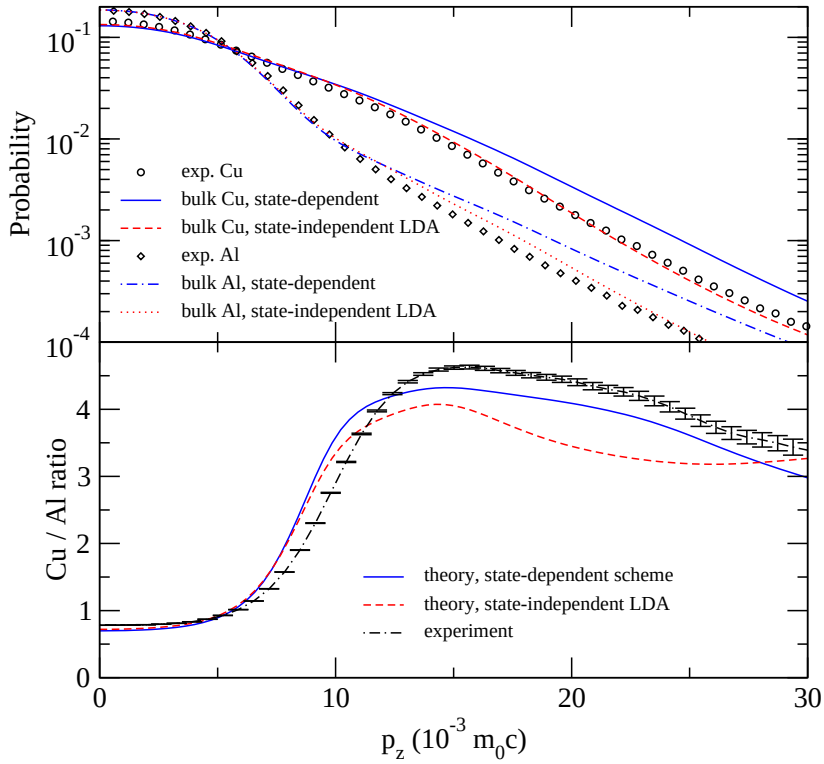

Figure 3: Calculated and experimental Doppler broadening spectra of bulk Cu and bulk Al (above) and the Cu/Al ratio spectrum (below). The computational results are calculated using both the state-independent LDA scheme and the state-dependent scheme for momentum densities. The experimental data is from Ref. [62]. From Publication II.

2. When using the ratio representation the results calculated using the state-dependent scheme are in excellent agreement with experiment no matter which two spectra are chosen. Especially at high momenta they are in much better agreement than the state-independent LDA results.

Figure 3 shows theory-experiment comparisons for bulk Cu and bulk Al. Also the Cu/Al ratio spectrum is shown. The state-independent LDA model reproduces the absolute intensities at high momenta better but the spectra oscillate around the experimental ones. In the ratio spectrum the oscillations lead to a qualitatively wrong behavior at high momenta whereas in the result calculated using the state-dependent model the systematic

errors are completely canceled.

The state-independent LDA model of Eq. (26) enhances the Umklapp components of the Bloch states in a very non-trivial way because of the position-dependence of the enhancement factor. This leads to oscillations in the ratio spectra. The smaller intensity at high momenta results from the fact that $\psi_+(\mathbf{r})\psi_j(\mathbf{r})\sqrt{\gamma(n_-(\mathbf{r}))}$ is broader in the real space than $\psi_+(\mathbf{r})\psi_j(\mathbf{r})$ (near the nuclei where the electron density is higher $\gamma(n_-)$ decreases towards unity while in the interstitial regions it is of the order of 4) and hence the corresponding momentum distribution is narrower than in the IPM leading to a lower intensity at high momenta.

In our applications the chemical identification of, for example, impurity atoms around vacancies is very much based on the annihilation signal from core electrons and on the Umklapp components due to the valence electrons. The computed and measured spectra are compared up to momenta as high as $40\times10^{-3}\,m_0c$. Therefore, the momentum dependence of the enhancement inside the first Brillouin zone is not of utmost importance. More important is how the enhancement of the Umklapp components is described. In the state-dependent model [Eq. (27)] they are enhanced with the same factor as the $\mathbf{G} = 0$ component as in the IPM. The state-dependent scheme enables one to treat all electronic states in a similar fashion while still getting a reasonable agreement with the experiment. This is also in the spirit of DFT because in general all the electronic states are treated similarly as the total densities are the fundamental quantities. The problem with the too high intensity in the state-dependent model at high momenta can be circumvented by plotting ratio spectra.

In order to be able to compare the three-dimensional momentum density of annihilating electron-positron pairs, $\rho(\mathbf{p})$, with experiments it has to be projected to one or two dimensions,

$$\rho(p_z) = \int\int dp_x dp_y\, \rho(\mathbf{p}), \tag{29}$$

$$\rho(p_x, p_y) = \int dp_z\, \rho(\mathbf{p}). \tag{30}$$

Depending on the method the experimental spectrum is measured with the spectrum of Eq. (29) is termed either the Doppler broadening spectrum or the 1D-ACAR spectrum. Equation (30) corresponds to the 2D-ACAR spectrum. The computational momentum distributions have to be convoluted with the experimental resolution function before comparing them with experimental ones.

In practice most of the theory-experiment comparisons in the thesis are done by plotting ratios of two Doppler spectra or the so-called ratio-difference spectrum (relative difference to the corresponding bulk spectrum). In this representation the non-saturation trapping seen in experiments affects only the scaling of the spectrum and not its shape (for further motivation see Publication V).

The experimentally measured line shapes of the Doppler-broadened 511-keV line are conventionally described using so-called S and W parameters [1] which are presented graphically in Fig. 2. The S (central) parameter is the integral over the low-momentum region of the Doppler spectrum. In the case of the W (wing) parameter the integration is made over the high-momentum part. The counts in the central region are mainly due to annihilation with low-momentum valence electrons. At high momenta the intensity is mainly due to core electrons. Therefore, the S and W parameters can directly be associated with valence and core electrons, respectively.

3.3 Implementation: Projector augmented-wave method

The pseudopotential approximation is a commonly used method in DFT calculations. The idea is to replace one problem with another which is easier to solve but still contains the essential physics. The strong Coulomb potential of the nucleus and the effects of the tightly bound core electrons are replaced by an effective ionic potential acting on the valence electrons. This is necessary because the wave functions are orthogonal against one another and around the nuclei this requirement manifests itself by rapid oscillations in wave functions. These oscillations can not be described using a reasonable number of basis functions. The resulting pseudo wave functions in the pseudopotential method are soft and approximate the all-electron wave functions (the accurate Kohn-Sham wave functions) in an indefinite way meaning in practice that the information on the high-momentum Fourier components (Umklapp components) of the wave functions is lost. A method combining the accuracy of all-electron methods with the efficiency and flexibility of pseudopotential methods is the projector augmented-wave method by Blöchl [10]. It enables one to perform electronic-structure calculations using soft pseudo wave functions which can be represented with a modest number of plane waves. The information on the accurate all-electron wave functions is, however, also conserved because they can be reconstructed from the pseudo wave functions within the PAW method. In this thesis the

PAW method is for the first time applied to Compton profile calculations (Publication I) and to calculation of momentum densities of annihilating electron-positron pairs in defects in solids. The implementation is described in Publication II. Ishibashi [63] had already applied the PAW method to the calculation of coincidence Doppler spectra for bulk materials and later Uedono *et al.* have used the code by Ishibashi to study vacancy-type defects in SiGe [64] and in polycrystalline Si [65].

The idea behind the PAW method is to define a linear transformation between all electron (AE) wave functions (the accurate Kohn-Sham wave functions) and fictitious soft pseudo (PS) wave functions that can be represented using a plane-wave basis. The AE wave function is written as

$$|\Psi\rangle = |\tilde{\Psi}\rangle + \sum_i (|\phi_i\rangle - |\tilde{\phi}_i\rangle)\langle\tilde{p}_i|\tilde{\Psi}\rangle. \tag{31}$$

Above, $|\tilde{\Psi}\rangle$ is the PS wave function corresponding to the AE wave function $|\Psi\rangle$, and $|\phi_i\rangle$ and $|\tilde{\phi}_i\rangle$ are so called AE and PS partial waves, respectively, represented in radial grids around each ion and used to expand the AE and PS wave functions $|\Psi\rangle$ and $|\tilde{\Psi}\rangle$ locally around each nucleus

$$|\Psi\rangle = \sum_i |\phi_i\rangle c_i, \qquad \text{and} \qquad |\tilde{\Psi}\rangle = \sum_i |\tilde{\phi}_i\rangle c_i, \qquad \text{within } \Omega_R, \tag{32}$$

where Ω_R is the augmentation region (sphere) centered at site R. Above in Eq. (31), $|\tilde{p}_i\rangle$'s are localized projector functions which determine the expansion coefficients c_i as described below.

There is exactly one PS partial wave for each AE partial wave and the sets of expansion coefficients c_i are chosen to be identical for $|\Psi\rangle$ and $|\tilde{\Psi}\rangle$. The choice of the PS partial waves determines the softness of the resulting PS wave functions in the linear transformation [Eq. (31)]. The AE partial waves $|\phi_i\rangle$ are essentially atomic states and the PS partial waves $|\tilde{\phi}_i\rangle$ a set of soft functions that form a complete basis set in the space of the PS wave functions. The index i is a composite index consisting of the site index R, angular momentum indices l and m and an additional index k referring to the reference energy ε_{kl}. The partial waves are chosen so that the corresponding AE and PS waves match outside the augmentation region Ω_R (outside some radius r_c^l around the nucleus R).

The idea behind the transformation of Eq. (31) is represented in Fig. 4. The first term in the AE wave function is the corresponding PS wave function. The last term in Eq. (31) represents the difference between the AE and PS wave functions. Namely, the local expansions [Eq. (32)] are used to represent the AE and PS wave functions locally around each nucleus. In order

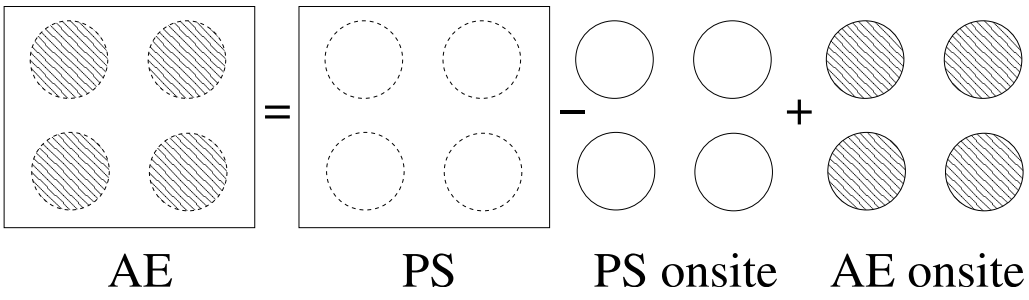

Figure 4: Division of the AE wave function into a PS term represented in a three-dimensional grid, and one-center PS and AE terms. [See Eq. (31).]

to arrive at a *linear* transformation between the AE and PS wave functions the expansion coefficients, c_i, have to be defined to be linear functionals of the PS wave functions, i.e., they can be written as inner products

$$c_i = \langle \tilde{p}_i | \tilde{\Psi} \rangle, \tag{33}$$

with suitable localized projector functions $|\tilde{p}_i\rangle$ that probe the local character of the PS wave function $|\tilde{\Psi}\rangle$. There is exactly one projector function per partial wave. The partial waves have to fulfill the duality condition $\langle \tilde{p}_i | \tilde{\phi}_j \rangle = \delta_{ij}$ so that the PS partial wave expansion of the PS wave function is complete in each augmentation region.

In practice the partial waves and projector functions are constructed as follows. The AE partial waves $|\phi_i\rangle$ are obtained from an all-electron calculation for a spherical reference atom and orthogonalized against core states. The PS partial waves $|\tilde{\phi}_i\rangle$ are represented using a set of soft basis functions (such as spherical Bessel functions as in Ref. [42]). The choice of the PS partial waves is not unambiguous. The transformation between the AE and PS wave functions and the softness of the resulting PS wave functions depend on it. The last step is to construct the projector functions $|\tilde{p}_i\rangle$. Soft preliminary functions are orthogonalized to the PS partial waves using a Gram-Schmidt-like scheme.

The power and accuracy of the PAW method in practical calculations is based on Eq. (31) which enables one to directly express the total energy functional in terms of the PS wave functions $|\tilde{\Psi}\rangle$. The PS wave functions are then used as variational quantities and one obtains modified Kohn-Sham equations which can easily be solved using plane-wave expansions. In the pseudopotential method there is no similar correspondence between the PS wave functions used in the computation and the accurate Kohn-Sham wave functions as in the PAW method.

As there is no built-in norm conservation requirement for the PS wave functions, so-called compensation (or augmentation) charges are used. They are localized charges placed at the sites of the nuclei. Their shapes and magnitudes are chosen so that the sum of the PS and compensation charge densities, $\tilde{n} + \hat{n}$, has inside the augmentation region the same multipole moments as the exact all-electron charge density n. Due to this trick also the interactions of one-center parts between different sites vanish and the total energy functional is of the form

$$E = \tilde{E} + E^1 - \tilde{E}^1. \tag{34}$$

The one-center terms E^1 and $\tilde{E}^1$ are evaluated on radial grids centered around each ion whereas the term $\tilde{E}$ is evaluated in the plane-wave grid. The expressions of all functionals, expectation values etc. in the PAW method are always similar to those of Eqs. (31) and (34) in the sense that first there is a PS term evaluated in plane-wave grid and then one-center terms related to AE and PS wave functions with plus and minus signs, respectively.

The compensation charges are utilized also in the positron calculations of this thesis. Since evaluating the AE valence charge density is difficult even with the help of the PAW method the Coulomb potential due to the AE charge density is approximated with the Coulomb potential due to the sum of the PS charge density and the compensation charges (see Publication II). The resulting potential matches the AE potential everywhere except inside the compensation charges. There the potential is so repulsive for the positron that this approximation has, in practice, no effect on the accuracy of the positron state.

In the momentum density calculations we first perform a standard PAW calculation from which we get the PS wave functions $|\tilde{\Psi}\rangle$. The AE wave functions $|\Psi\rangle$ are then reconstructed using the transformation of Eq. (31). This is in practice done in reciprocal space (see Publication I). This way no additional FFT's (fast Fourier transformations) have to be performed in Compton profile calculations. We control the convergence of results by setting a momentum cutoff for the AE wave functions. Finally, the AE wave functions are used to construct the three-dimensional momentum density $\rho(\mathbf{p})$ according to one of Eqs. (22), (26) or (27).

The effect of the linear transformation of the PAW method is demonstrated in Fig. 5 in the case of bulk Cu and especially the $3d$ states. The PAW method enables the use of very soft PS wave functions thereby making the calculations efficient and enabling one to study, for example, first-row elements, transition metals and rare-earth elements. Once the AE wave

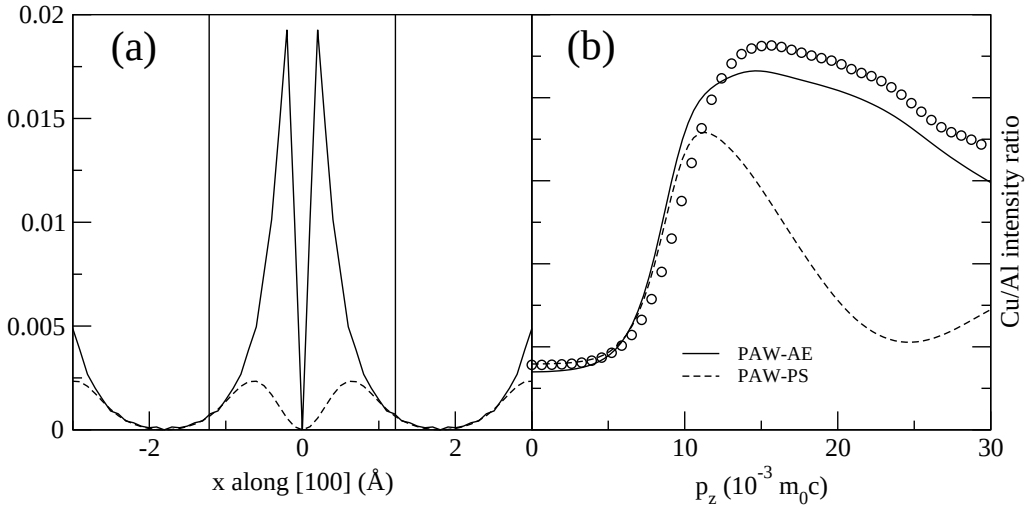

Figure 5: Effect of the AE wave function reconstruction in the case bulk Cu. (a) The Γ point AE and PS wave functions of a $3d$ state plotted in the real space. The Cu nucleus is at the origin of the x-axis. (b) The effect of the reconstruction on the Doppler spectrum (ratio to bulk Al). The theoretical Doppler broadening data is from Publication II and the experimental data from Ref. [62]

functions are reconstructed the information on the high-momentum Fourier components of the wave functions is regained. Especially when studying vacancy defects in semiconductors for which large supercells are needed the benefits of the PAW method become obvious. It offers as good computational efficiency and flexibility as the best pseudopotentials but with all-electron accuracy. The good controllability of the basis is another good property. Plane-waves are a natural basis for momentum density calculations. Also the fact that the PAW method enables a full-potential treatment can be important for a wide variety of nonmetallic systems.

Our PAW momentum density implementation is based on the one in the plane-wave code VASP (Vienna *Ab-initio* Simulation Package) [66, 67, 42] and VASP is used in the electronic structure calculations throughout this thesis. The positron state and some of the positron annihilation characteristics are calculated using the so-called Doppler package of the MIKA project [68]. The positron state is solved in the real space using the Rayleigh quotient multigrid solver described in Ref. [69]. In the positron calculations we treat the core electrons by an atom code based on DFT and LDA. In the cal-

culation of core electron contribution to Doppler spectra the positron wave functions are described by isotropic parametrized interpolation forms fitted to the results of LMTO-ASA (linear-muffin-tin-orbital method within the atomic-spheres approximation) calculations. We use a modified 4-parameter expression [70] of the form by Alatalo *et al.* [60] (see also Publication II).

4 Applications

This section presents a closer overview of the most important applications in the thesis.

4.1 Compton profile calculations

Compton scattering is inelastic x-ray scattering at large energy and momentum transfers. For a recent review see Ref. [71]. It can be used to probe the ground-state electronic structures of solids. In the impulse approximation the Compton-scattering cross-section is related to the one-particle electron momentum density of the material. Modern crystal spectrometers and third generation synchrotron sources enable momentum resolution high enough for Fermi surface studies. The technique enables one also to study the local structure and dynamics of liquids, for example, hydrogen-bonding in water (see, for example, Ref. [72]). In Publication I of this thesis both experimental and theoretical Compton scattering data were used as benchmarks for the PAW momentum density implementation. This is the first logical step because in Compton profile calculations one does not need to solve the positron state and worry about the electron-positron correlations. Furthermore, it is an important step because the PAW method can have many applications also in Compton profile calculations.

We used the LDA with no correlation corrections. We found that the method gives results comparable to other well-established all-electron approaches. The Compton profiles of Si, Li, Al and the water dimer $(H_2O)_2$ were calculated and compared to experimental results and other all-electron results in the literature or in the case of the water dimer to a calculation made with localized basis functions. For Si we get a nice agreement with both experiment [73] and calculations [74] in which AE wave functions were reconstructed from a calculation made using conventional norm-conserving pseudopotentials. For Li we get a bad agreement with the experiment [75] but a perfect match with an earlier LDA calculation [75] made using the Korriga-Kohn-Rostoker (KKR) method. Li is a difficult system because of either its strong correlation effects due to low electron density or its softness which makes the effects of thermal disorder important. For Al we get a nice agreement with both experiment and previous LDA calculations [76]. Figure 6 shows the calculated directional Compton profiles and their derivatives compared with the experiment. Water is an example of a disordered, non-crystalline system to which the PAW method and the supercell approx-

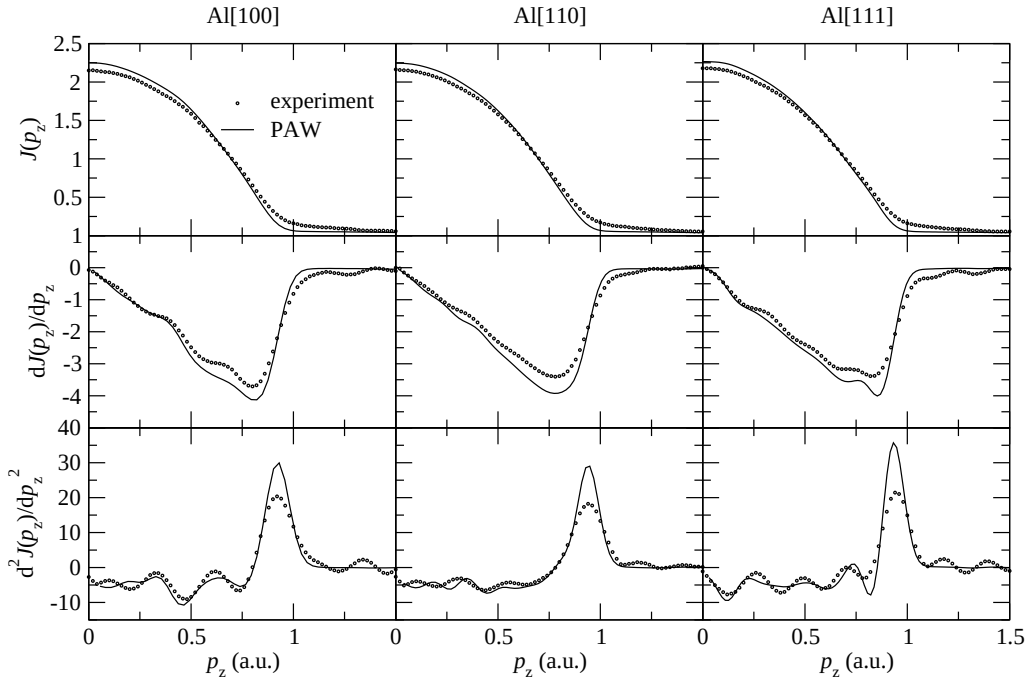

Figure 6: Valence Compton profiles of Al along different directions (the first row). Also their first and second derivatives are shown (the second and third rows). The experimental valence Compton profiles (Ref. [76]) have been obtained by subtracting the KKR core profile [76] from the measured ones. From Publication I.

imation can be applied. For the water dimer, the agreement with results we calculate with a code based on a localized basis set is satisfactory.

In conclusion, the PAW method applied to Compton profile calculations gives results that are comparable in numerical accuracy with results of other all-electron calculations made within the LDA using methods such as KKR or the full-potential linearized augmented plane wave method. The method can be applied as well for calculating Compton profiles of molecular systems as those of crystalline solids.

The first real application [77] of the PAW method in the field of Compton scattering has recently been published. In that work the authors studied experimentally the isotope quantum effects in the electron momentum density of water. Also an ab-initio model was applied in which deuterated water was studied using a supercell approach and Car-Parrinello molecular dynamics

simulations. Snapshots of the molecular dynamics simulations were used when calculating the time-averaged Compton profile with the PAW method and the VASP code.

4.2 Highly Sb-doped Si

Publication III deals with n-type doping of Si. In today's semiconductor components the required charge carrier concentrations are so high that the dopant concentrations are already of the order of 1%. At this very high doping level the free electron concentration in n-type Si has been found to saturate at $< 5 \times 10^{20}$ cm^{-3} regardless of the doping density [78, 79]. In Publication III highly Sb-doped Si samples grown using molecular beam epitaxy (MBE) were studied with positrons in order to clarify the role of vacancy defects in the electrical compensation. Our calculations were used in the interpretation of experimental Doppler broadening data. Statistical analysis of recent electron microscopy experiments [80] shows that the primary deactivating defects in highly Sb-doped Si contain 2 Sb atoms which are second-nearest neighbors to each other. In a subsequent study [81] the off-column displacements of Sb atoms measured with the annular dark-field scanning transmission electron microscope (ADF-STEM) were compared with structural models obtained using first-principles calculations. The models included defects such as the complex formed by a vacancy (V) and two substitutional Sb atoms, V-Sb_2, and the donor-pair [82] [DP(i)] and donor-pair vacancy interstitial [81] [DP(i)-V-I] defects. The DP(i) defects consist of 2 substitutional donor atoms at second- or fourth-nearest-neighbor sites ($i = 2, 4$). In the DP(i)-V-I defects there is also a displaced Si atom that forms a Si vacancy and a Si interstitial, I. Of these defects only the V-Sb_2 complex contains a sufficiently large open volume for positron trapping. Based on the measured off-column displacements and the ones calculated for the model defects using DFT calculations the dominant deactivating defect was argued to be the DP(2)-V-I defect. The other candidate defects were rejected because of large calculated inward relaxations of Sb atoms from their ideal lattice sites and their higher formation energies. Here one must note that the ADF-STEM measurements can not detect the possible vacancies in the vicinity of the Sb atoms.

In Publication III the same MBE-grown highly Sb-doped Si samples as in Refs. [80, 81] were studied using positron annihilation spectroscopy and a low-energy positron beam. Our theoretical calculations were used to analyze measured Doppler broadening spectra. The first step before

trying to identify the defects in the MBE grown samples under investigation was to study reference samples with large concentrations of V-Sb_1 and V-Sb_2 defects created by electron irradiation and annealing. The obtained Doppler spectra were compared with the theoretical ones. Figure 7 shows the comparison. The agreement between the experiment and the theory is very good at all momentum regions. The peak at around 14×10^{-3} m_0c is due to $4d$ electrons of Sb and its height correlates with the number of Sb atoms surrounding the vacancy. Much of the discrepancy is due to the approximate geometries of the V-Sb_i defects. Namely, in the modeling ideal (unrelaxed) defect geometries were used. Actually, at least for V-As_i defects this seems to be a good approximation (see Publication VII). The effect of the position of the Sb atom is demonstrated for the V-Sb defect in Fig. 7. The Sb atom is displaced +5% (−5%) of the Si nearest-neighbor distance outward (inward).

Based on the comparison in Fig. 7 the calculations were found to reliably describe the annihilation characteristics of the vacancy-Sb complexes. Next, similar calculations were carried out for the DP(i)-V-I defects and for divacancy-Sb complexes, V_2-Sb_i, because the S line-shape parameters measured from the MBE-grown samples suggested that there are vacancy defects present with a larger open volume than a monovacancy. These data were used to interpret the experimental Doppler broadening data measured for the MBE grown samples. It turns out that no single defect type is able to explain the experimental Doppler broadening data. Our comparisons suggest that the defects trapping positrons consist of mono- and divacancies surrounded by one or two Sb atoms. After a heat treatment at 575 K the contribution of Sb $4d$ electrons strongly increases suggesting that the number of Sb atoms neighboring vacancies also increases. Also the measured S parameter increases with increasing annealing temperature suggesting that the vacancy clusters grow in size. The highly Sb-doped MBE Si is thus atomically metastable after the growth; the grown-in vacancies mediate the formation of larger vacancy-Sb clusters by annealing already below the growth temperature.

The vacancy concentrations determined in Publication III for the samples with various Sb concentrations show that the concentrations of the open-volume defects with one or two neighboring Sb atoms are high enough to be important for the compensation of Sb donors. The results are in agreement with the electron microscopy studies, in which Sb impurities occur either in isolation or in pairs [80]. Also, the presence of defects like V-Sb_2 and V_2-Sb_2 is compatible with diffusion data. The V-Sb_1 defect is

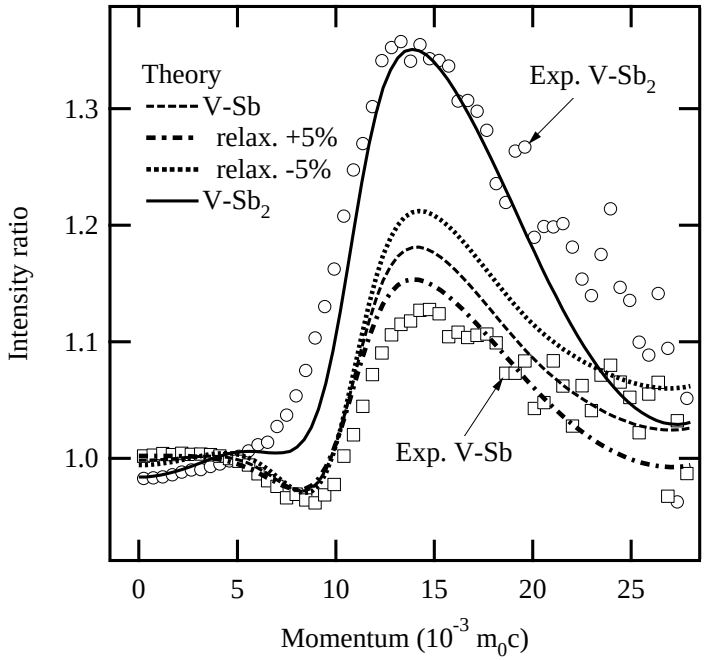

Figure 7: Momentum density along the [111] direction at the irradiation-induced V-Sb_1 and V-Sb_2 defects, as scaled to that of the vacancy-phosphorous pair. The lines are obtained from theoretical calculations, showing also the influence of lattice relaxation (fraction of the Si-Si bond length, Sb atom relaxed only). From Publication III.

mobile at the growth temperature of 550 K. Its migration leads to formation of more stable complexes such as V-Sb_1 or V_2-Sb_2 when it encounters an isolated Sb atom or another V-Sb_1. Thus, no complexes with 3 Sb atoms can form.

4.3 Impurity decoration of Ga vacancies in GaN

Publication IV examines the possibility of distinguishing neighboring elements in the Periodic Table of elements using positron annihilation spectroscopy. The specific system is the Ga vacancy in GaN. The effect of O atoms neighboring Ga vacancies on the Doppler broadening spectrum was studied using O-doped n-type GaN samples grown by hydride vapor phase epitaxy (HVPE). Annealing experiments show that a V_{Ga} formed in growth is more stable than one formed in electron irradiation [83]. Therefore, a Ga

vacancy in the O-doped HVPE samples is thought to be complexed with an impurity atom. The positron lifetime is too insensitive to tell if the Ga vacancy is isolated or complexed. The reference sample representing a clean Ga vacancy was undoped HVPE GaN which was irradiated with electrons in order to produce vacancies. Doppler broadening spectra were calculated for the clean Ga vacancy, for a vacancy complexed with O, V_{Ga}-$\mathrm{O_N}$, and for the divacancy V_{Ga}-$\mathrm{V_N}$. Figure 8 shows the experimental spectra (ratios to bulk GaN) measured for the clean Ga vacancies and the Ga vacancies in the O-doped HVPE samples. The theoretical data for the model defects is shown below the experimental data. The PAW method and self consistent relaxations are essential in this study because the effect of the ionic relaxations on the calculated Doppler spectrum can be comparable to that due to the differences in the electronic structures of O and N atoms. Furthermore, since the electronic states derived from O and N $2s$ and $2p$ atomic orbitals contribute the high-momentum part of the Doppler spectrum it is important to describe them accurately.

The experimental data for the electron irradiated sample is reproduced well at all momentum regions by the computation supporting the identification of an isolated Ga vacancy. The effect of the O atom neighboring the vacancy is to enhance the intensity at high momenta. The behavior of the experimental HVPE data is similar.

We also studied the effect of possible H atoms at the Ga vacancies on the Doppler broadening spectra by calculating the spectra for V_{Ga}-H and V_{Ga}-2H. The atomic configurations were taken from Ref. [84]. In GaN grown by metal-organic chemical vapor deposition (MOCVD) the concentrations of residual O and H atoms are high. The experimental data from a MOCVD sample is also shown in Fig. 8. The intensity at high momenta is even larger than in the case of the HVPE data. The behavior is similar to that in the computational data for the H-decorated Ga vacancies.

In conclusion, the comparison in Fig. 8 shows that the measurement of momentum density is sensitive enough to distinguish between O and N atoms neighboring the Ga vacancy. We identify the isolated Ga vacancy in undoped electron irradiated GaN and show that in O-doped HVPE GaN the the Ga vacancy is complexed with the O atom forming V_{Ga}-$\mathrm{O_N}$ pairs. In MOCVD material the Ga vacancy is likely be decorated by both oxygen and hydrogen. In this case, however, the discrimination between O and N is obscured by the stronger contribution of H atoms at high momenta.

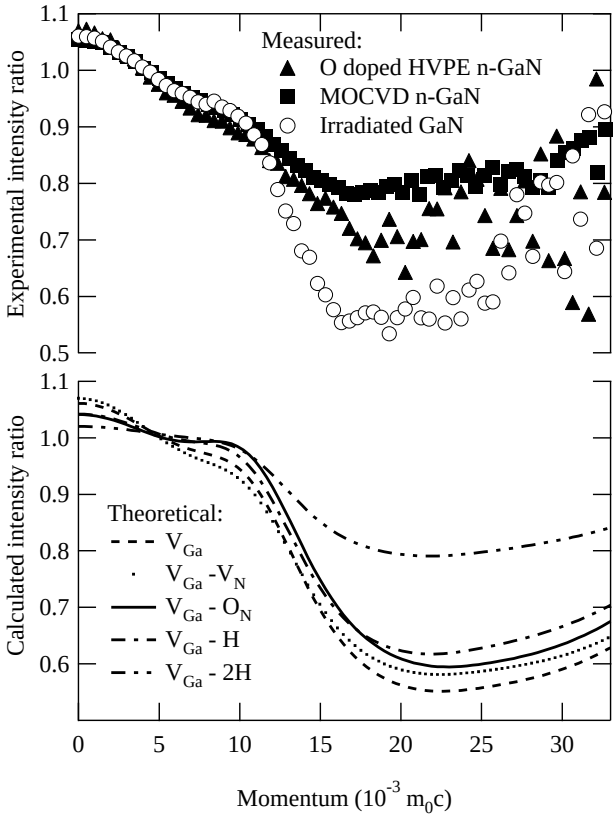

Figure 8: Measured (above) and calculated (below) momentum distribution curves for different types of GaN samples and defects. The spectra are shown as rations to the data obtained for the defect-free GaN lattice. From Publication IV.

4.4 Positron localization effects on the Doppler broadening of the annihilation line

When a delocalized positron gets trapped at an open volume defect the trapping has at least the following two well-known effects on the measured Doppler broadening spectrum. First of all, the electron density sensed by the positron is lowered compared to the value in perfect bulk and the positron is mainly in contact with low-momentum valence electrons. This is seen in the spectrum as increase in the hight of the peak at $p_z = 0$. Secondly, the overlap of the positron state with high-momentum core electron states is

decreased leading to a decreased intensity at high momenta. Publication V discusses in addition to these effects also a third effect which is visible only in metals since its mechanism is related to the Fermi surface. When a positron gets trapped at a vacancy defect its momentum distribution is broadened according to the Heisenberg uncertainty principle $\Delta x \Delta p \geq \hbar/2$. The effect of the quantum confinement is to smear the Fermi surface because the increased positron momentum enhances the electron-positron momentum density at momenta beyond the Fermi momentum. This effect in addition to the others is demonstrated in Publication V both experimentally and computationally using Al as an example. Previously, Saniz *et al.* [85] have demonstrated the combined effect due to confinement of both electrons and the positron in a quantum dot using a simple potential well model. Chiba *et al.* [86] argue that they see with the 2D-ACAR technique a Fermi surface broadening effect in bcc Cu nanoclusters embedded in Fe. Weber *et al.* [87] have studied the energy-cap scaling in semiconducting CdSe quantum dots as the function of quantum dot diameter. The annihilation line shape shows a smearing at the boundary of the Jones zone. The broadening can be understood with the help of a one dimensional model [88] that predicts the Jones zone broadening to be proportional to the energy band gap of the material. In the case of the CdSe quantum dots the diameter of the dot determines the band gap and thereby the smearing.

Figure 9 shows two experimental spectra measured from two different Al samples. The sample corresponding to Fig. 9(a) contains quenched-in thermal vacancies whereas the one of Fig. 9(b) has vacancies created by sample deformation. The defect-related positron lifetimes of these samples are 235 and 225 ps, respectively. The vacancies in the latter sample have a smaller volume because they are stabilized by strain fields of the deformation-induced dislocations. The above-mentioned effects of positron trapping are clearly visible. (*i*) The peak at $p_z = 0$, (*ii*) the reduced core annihilation reflected in the negative value of the curves at high momenta and (*iii*) the peaks at around $8 \times 10^{-3}\ m_0 c$ just above the Fermi momentum. In the representation used in Fig. 9 the possible non-saturation trapping affects only the scaling of the curve and not its shape (see the discussion in Publication V). The shape of the curve is determined by the morphology of the positron traps. The two experimental curves in Fig. 9 can not be scaled to a common master curve indicating that the positron traps in the samples are different.

The solids lines in Fig. 9 are computational results for monovacancies in Al. The experimental data is fitted with computational data using the

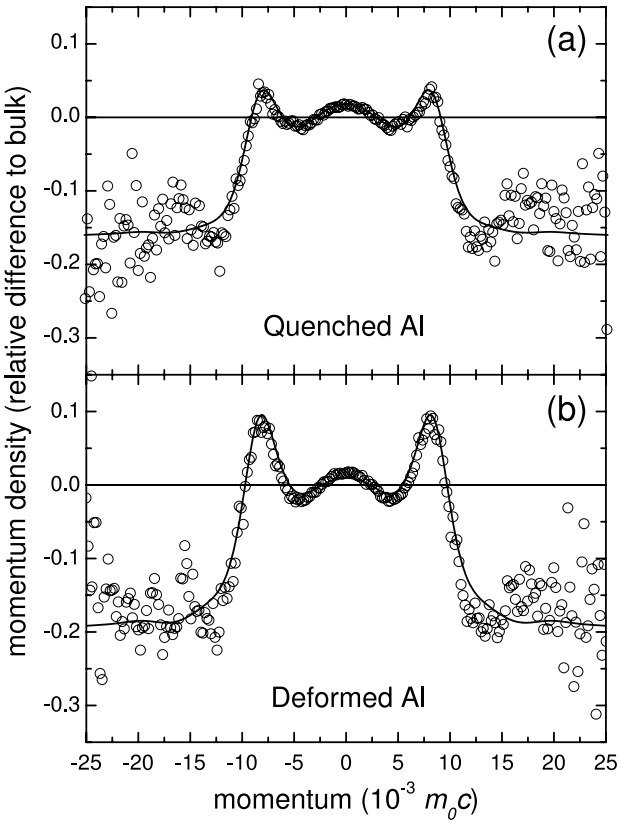

Figure 9: Coincidence Doppler broadening spectra for defected Al (relative differences to annealed Al). The solid lines are the results of the calculations (see the text). From Publication V.

(experimental) trapping fraction F (the fraction of positrons annihilating at vacancies) and the (computational) volume of the vacancy as fitting parameters. The first one affects only the scaling of the curve and the latter one determines the shape. The relaxations of the atoms neighboring the vacancy are (a) 0% and (b) 4% inward (compared to the Al nearest-neighbor distance). The computed lifetimes are 234 and 211 ps, respectively. The fitted trapping fractions are in excellent agreement with the ones obtained with the standard trapping model from positron lifetime measurements.

In Publication V model calculations are used also to further demonstrate the different effects positron localization has on the Doppler broadening spectrum. The calculations enable one to determine annihilation parameters as a function of the relaxation of the vacancy and simultaneously

separately monitor changes in the annihilation rates and momentum densities of annihilating electron-positron pairs due to valence and core electrons and also the momentum-density of the positron itself. The Fermi surface smearing effect can also be demonstrated separately from the other two effects by convoluting the momentum distribution for bulk Al with Gaussian functions corresponding to different degrees of positron localization.

4.5 Quantitative chemical analysis of vacancy-solute complexes in metallic solid solutions

The motivation for Publication VI is to study the possibility of quantitative chemical analysis of vacancy-solute association in metallic solid solutions using Doppler broadening spectroscopy. The specific systems are the technologically important Al-Cu, Al-Cu-Mg and Al-Cu-Mg-Ag alloys. A few years ago Somoza *et al.* [89] proposed a method in which the signal due to both Al and solute atoms, for example Cu, around vacancies in the alloys is described using the spectra measured for vacancies in the corresponding elemental metals. The relative concentrations of the solute atoms around the vacancies are then obtained using a linear fitting procedure. We used the modified procedure due to Ferragut [90] that also takes into account the possibility of non-saturation trapping of positrons. The scheme is described below.

The equation used to fit a spectrum measured for an Al-based alloy is written as

$$\rho^{\mathrm{fit}}(p) = (1-F)\rho_{\mathrm{Al}} + F\sum_i C_i \rho_i^{\mathrm{vac}}(p), \tag{35}$$

where ρ_{Al} is the bulk spectrum, $\rho_i^{\mathrm{vac}}(p)$ is the spectrum corresponding to saturation trapping at monovacancies in the elemental metal i (for example Al, Cu, Mg, or Ag), F is the trapping fraction, and C_i's are the corresponding relative concentrations fulfilling the normalization condition $\sum_i C_i = 1$. The fitting parameters in Eq. (35) include F, and the C_i's of which one is linearly dependent on the others. The spectra used in Eq. (35) can be either measured ones (see, for example, Refs. [91, 92, 93, 94]) as always in the past or originate from theoretical calculations. What was not clear on the basis of the original experimental construction was how well the spectra measured for vacancies in elemental metals correspond to the signal due to corresponding impurities around vacancies in Al-based alloys and how well the relative concentrations of solute atoms neighboring vacancies, C_i, are deduced from the spectra in the fitting. This problem arises mainly from

the different lattice constants of the host and the solute metals and it can only be addressed using theoretical calculations. In principle calculations would enable one to use more realistic vacancy-solute complexes than the systems used in the fitting. However, it turns out that this kind of fitting is not stable due to linear dependencies in the fitting functions and the result will depend on how they are chosen. Moreover, we find by simulations that using Eq. (35) one obtains the relative concentrations of solute atoms with reasonable accuracy.

The fitting procedure was tested by mimicking experimental spectra with the ones computed for vacancy-solute complexes with specific numbers of surrounding solute atoms. Also as fitting functions we used consistently the calculated ones. Although we had a saturation trapping ($F = 1$) in our model calculations we kept F as a free parameter in order to see how stable the fitting really is.

We considered vacancy defects in binary Al-Cu, ternary Al-Cu-Mg and quaternary Al-Cu-Mg-Ag alloys. Our findings can be summarized as follows. Using the fitting procedure described above the accuracy is usually better than 0.5–1 atoms of the 12 nearest-neighbor atoms of the vacancy in Al. In some cases the fitting may lead to a slightly wrong value for F but because of compensation effects the relative concentrations are still reproduced well. However, adjacent atoms of the Periodic Table having similar core electron structures (such as Mg and Al) cannot be distinguished reliably. Figure 10 shows a model spectrum for a vacancy in Al surrounded by 2 Cu, 2 Ag and 1 Mg solute atoms and the corresponding fit with its components. The concentrations obtained from the fit are in this case equivalent to 2.08, 2.63, and 0.71 surrounding Cu, Ag, and Mg atoms, respectively, while the fitted trapping fraction F is 0.963.

The fitting procedure is justified also in the sense that the characteristic signal of different solute atoms seems to depend linearly on the number of the atoms around vacancies and on the other hand the annihilation signals of defects with given numbers of surrounding solute atoms are not dependent on the atomic configuration. This enables one also to try to reproduce the experimental annihilation signal with the spectrum computed for a single model system. The number of neighboring solute atoms then directly correspond to the average one in the sample.

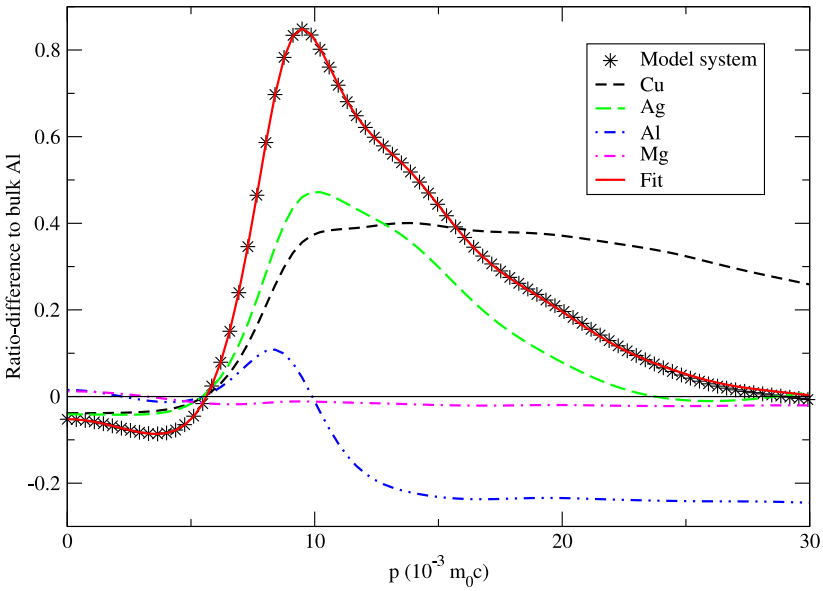

Figure 10: Spectrum for a model vacancy defect in an Al-Cu-Ag-Mg alloy with 2 Cu, 2 Ag and 1 Mg nearest-neighbor solute atoms surrounding the vacancy. The spectrum is fitted using the spectra for vacancies in Cu, Ag, Al and Mg and that of bulk Al. The contributions of the different elements as well as the resulting spectra are shown. The data is from Publication VI.

4.6 Energetics of trapped positron states

Publication VII studies in more detail the energetics of the positron trapping process and the ionic relaxations taking place when a positron gets trapped at a vacancy defect. A variety of different kinds of solids such as close-packed and body-centered cubic metals, compound and elemental semiconductors are considered. We discuss the positron trapping energies at monovacancies in these materials (the energy released in the trapping process) and the effect of the localized positron on their volumes, point symmetries and electronic structures.

In the conventional scheme the total energy of a system of a positron in an ionic lattice is the sum of the DFT total energy for the electron-ion system and the positron energy eigenvalue. The trapping energy of a positron to a defect is defined as the difference between the total energies of the initial and final states,

$$E_t = \Delta E_{\mathrm{tot}} = (E + \varepsilon^+_{\mathrm{bulk}}) - (E_{e^+} + \varepsilon^+_{\mathrm{defect}}) = (\varepsilon^+_{\mathrm{bulk}} - \varepsilon^+_{\mathrm{defect}}) - (E_{e^+} - E), \quad (36)$$

where $\varepsilon^+_{\rm bulk}$ and $\varepsilon^+_{\rm defect}$ are the positron energy eigenvalues in the delocalized bulk and localized defect states, respectively, and E and E_{e^+} are the energies of the defect supercell (electron-ion system) without and with a localized positron at the vacancy. The last form in Eq. (36) shows that the trapping energy consists of the decrease in the positron energy eigenvalue and the increase in the strain energy stored in the ionic lattice.

The differences in the energetics are found to be large between different materials. The extrema in the one end are elemental semiconductors such as Si and the other end close-packed metals. In Si the lowering of the positron energy eigenvalue is of the same order as the increase in the strain energy of the lattice leading to a vanishingly small trapping energy. This is true for a wide range of ionic positions which makes the energy landscape of the Si vacancy-positron system extremely flat. Figure 11 shows a comparisons between the energy landscapes of an Al vacancy and a neutral Si vacancy. The energies of the electron-ion systems (the uppermost curves) and the positron energy eigenvalues (the lowest curves) as well as their sums, the total energies of the systems (the curves in the middle), are shown as a function of the relaxation of the nearest neighbor ions. The relaxations are constrained to symmetric breathing-mode relaxations. The energy zero is chosen to be the total energy of the vacancy and the trapped positron with ions relaxed without positron-induced forces. Then the uppermost curves correspond also to the total energy of the vacancy and a delocalized positron. The smallest relaxations correspond to the structures obtained without the localized positron and the largest ones with a localized positron at the vacancy. In fact, in the case of the Si vacancy the isolated vacancy does not even trap the positron. Therefore, all the curves meet at the strongest inward relaxation in Fig. 11(b).

In addition to trapping energies Publication VII presents information on the positron-induced relaxations. The effect of the positron on the volume of the vacancy is especially large in elemental semiconductors. Although the positron-induced changes are smaller in the case of metal vacancies the effect on the computed annihilation characteristics are still significant. In the case of vacancies in semiconductors the localized positron effectively cancels all the Jahn-Teller distortions observed without the localized positron. We also examined the effect of the positron on computed ionization levels of the vacancy defects in semiconductors. The effect was shown to be minor although the positron-induced relaxations are large. Therefore, we do not expect the localized positron to change the charge state of the defect prior to its annihilation. In addition to the Si vacancy the vacancy in Ge as

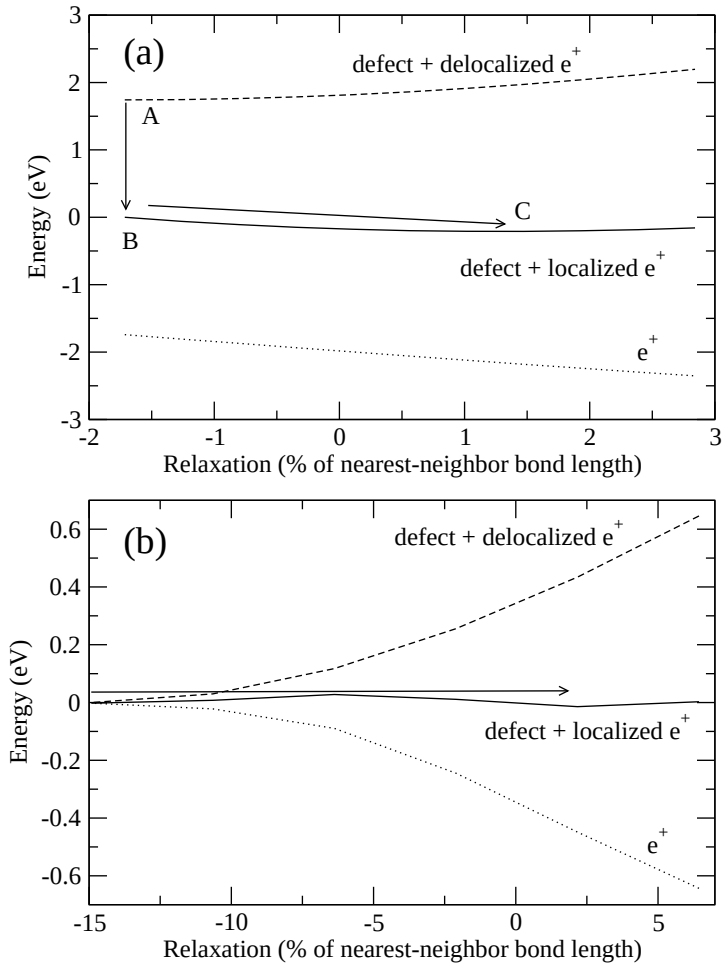

Figure 11: Configuration-coordinate diagram for (a) the monovacancy in Al and (b) the neutral monovacancy in Si. The dotted lines show the positron energy eigenvalue (relative to the one in perfect bulk), the dashed lines the energy of the lattice and the delocalized positron and the solid line the total energy of the defect-positron system as functions of the relaxation of the vacancy. Positive (negative) sign denotes outward (inward) relaxation. The points A, B and C denote different stages in the positron trapping process. From Publication VII.

well as the As vacancy in GaAs seem difficult to model because we found the positron trapping to be energetically unfavorable and even a metastable configuration with trapped positron state was not found. The N vacancy in GaN does not seem to have a bound positron state at all. Although the results may in some borderline cases as Si be even qualitatively incorrect Publication VII demonstrates that there are some important trends in the energetics of positron trapping between different kinds of materials.

5 Summary and conclusions

In this thesis practical methods for modeling momentum distributions of positron annihilation radiation in solids were developed and applied to the interpretation of positron annihilation experiments, especially to chemical identification of vacancy defects in semiconductors and in metallic alloys. The same methods were applied also to Compton profile calculations which in this thesis mostly served as benchmarks for the method. Future applications, however, are expected also in this field.

In Compton profile calculations the PAW method was shown to give results comparable in numerical accuracy with other all-electron methods (Publication I). The approach was further tested in the calculation of momentum distributions of annihilating electron-positron pairs in Publication II. Also different approximations for the calculation momentum distribution of positron annihilation radiation. were compared in the case of perfect bulk systems. The so-called state-dependent scheme turned out to reproduce the experimental results when the data was represented by plotting ratio spectra. When applied with the Boroński-Nieminen LDA for electron-positron correlation effects the scheme suffers from overestimated intensity at high momenta. The state-independent LDA scheme by Daniuk *et al.* reproduces the absolute intensities well but the computational spectra oscillate about the experimental one which leads to unphysical features in the ratio spectra. When used with the state-independent scheme the GGA by Barbiellini *et al.* describes both the absolute intensities and the shapes of the ratio spectra well. However, in some cases it fails to predict the ratios as successfully as the Boroński-Nieminen LDA and, furthermore, it has the additional disadvantage that it involves one semi-empirical parameter.

The methods were applied to the identification of vacancy-impurity complexes in semiconductors in Publications III and IV by interpreting experimental Doppler broadening data. In Publication III we identified vacancy-impurity complexes in n-type highly Sb-doped Si grown by molecular beam epitaxy. In Publication IV calculations were used to demonstrate the effect of oxygen and hydrogen on the Doppler broadening signal of Ga vacancy in GaN.

In Publications V and VI the methods were applied to metallic systems, namely to Al and Al-based alloys. In Publication V calculations were used to demonstrate the effect of quantum confinement of the positron at a vacancy in a metal on the observed Doppler spectrum. Publication VI discussed the possibility of quantitative chemical analysis of vacancy-solute

association in Al-based alloys. Our results give support to a previously used analysis method in which the relative concentrations of solute atoms surrounding vacancies are fitted by describing their effect on the Doppler broadening spectrum by the signal of the vacancy in the corresponding elemental metal. The presence of up to three different types of impurity atoms may be discriminated as long as their core electron structures are sufficiently different.

In Publication VII especially the energetics of positron trapping and the interaction between the localized positron state and the ionic lattice were studied. We observed notable differences between metals, compound- and elemental semiconductors. In metals the energy stored in the ionic lattice is a minor contribution in the net energy balance whereas in the case of elemental semiconductors like Si the calculations indicate that in principle all the energy released in the trapping process could be stored in the lattice. Although the energy considerations based on our calculations are not fully in line with experiments the calculations clearly show that the interplay between the positron and the lattice is important in positron trapping especially in semiconductors.

In conclusion, plane-wave supercell calculations with the PAW method enable a very good numerical accuracy in momentum density calculations and are efficient enough for the study of small vacancy defects in semiconductors with reasonably large supercells. Also the forces on ions due to a localized positron can be taken into account which enables self-consistent determination of positron and electron densities and the ionic structure. There are numerous applications of the methods used in the thesis in defect identification using positron annihilation spectroscopy.

In the present calculations the numerical accuracy is not a limiting issue anymore. More important are the accuracies of the functionals of the DFT and the two-component DFT and the accuracy of the model used for the calculation of momentum distributions of annihilating electron-positron pairs. Especially the localized positron states and defect structures call for a better description. The novel DFT functionals may offer an improved description of the energetics of the semiconductor defects. Recent improvements [95] in trial wave functions used in variational quantum Monte Carlo calculations of electron-positron systems remove the previously existing problem of annihilation rates below the positronium value at low electron densities. In the future quantum Monte Carlo methods could possibly be applied to describe a localized positron in a model defect system with tens or even hundreds of atoms.

References

[1] R. Krause-Rehberg and H. Leipner, *Positron Annihilation in Semiconductors* (Springer-Verlag, Berlin, 1999).

[2] K. Saarinen, P. Hautojärvi, and C. Corbel, in *Identification of defects in semiconductors*, edited by M. Stavola (Academic Press, New York, 1998), Vol. 51A, p. 209.

[3] Y. Nagai, T. Chiba, Z. Tang, T. Akahane, T. Kanai, M. Hasegawa, M. Takenaka, and E. Kuramoto, Phys. Rev. Lett. **87**, 176402 (2001).

[4] Z. Major, S. B. Dugdale, R. J. Watts, G. Santi, M. A. Alam, S. M. Hayden, J. A. Duffy, J. W. Taylor, T. Jarlborg, E. Bruno, D. Benea, and H. Ebert, Physical Review Letters **92**, 107003 (2004).

[5] *Fermiology of High-T_c Superconductors*, edited by A. Bansil, A. J. Arko, R. Benedek, V. J. Emery, and L. C. Smedskjaer [J. Phys. Chem. Solids **52**, No. 11/12 (1991)].

[6] *Electronic Structure and Fermiology of High-T_c Superconductors*, edited by T. Takahashi, A. Bansil, and H. Katayama-Yoshida [J. Phys. Chem. Solids **53**, No. 12 (1992)].

[7] S. W. H. Eijt, B. Barbiellini, A. J. Houtepen, P. E. Mijnarends, and A. Bansil, Phys. Status Solidi C (2007), accepted for publication.

[8] P. J. Schultz and K. G. Lynn, Rev. Mod. Phys. **60**, 701 (1988).

[9] M. J. Puska and R. M. Nieminen, Rev. Mod. Phys. **66**, 841 (1994).

[10] P. E. Blöchl, Phys. Rev. B **50**, 17953 (1994).

[11] S. P. Ringer and K. Hono, Mater. Charact. **44**, 101 (2000).

[12] A. Dupasquier, G. Kögel, and A. Somoza, Acta Mater. **52**, 4707 (2004).

[13] M. J. Puska, C. Corbel, and R. M. Nieminen, Phys. Rev. B **41**, 9980 (1990).

[14] W. Brandt, in *Positron annihilation*, edited by A. T. Stewart and L. O. Roelling (Academic Press, New York, N.Y., 1967), p. 155.

[15] P. Hautojärvi and C. Corbel, in *Positron Spectroscopy of Solids, Proc. of the Int. School of Physics Enrico Fermi Course CXXV*, edited by A. Dupasquier and A. P. Mills (IOS Press, Amsterdam, 1995), p. 291.

[16] K. G. Lynn, J. R. MacDonald, R. A. Boie, L. C. Feldman, J. D. Gabbe, M. F. Robbins, E. Bonderup, and J. Golovchenko, Phys. Rev. Lett. **38**, 241 (1977).

[17] F. Tuomisto, V. Ranki, K. Saarinen, and D. C. Look, Phys. Rev. Lett. **91**, 205502 (2003).

[18] F. Tuomisto, K. Saarinen, D. C. Look, and G. C. Farlow, Phys. Rev. B **72**, 085206 (2005).

[19] R. M. Martin, *Electronic Structure: Basic Theory and Practical methods* (Cambridge University Press, Cambridge, 2004).

[20] P. Hohenberg and W. Kohn, Phys. Rev. **136**, B864 (1964).

[21] M. Levy, Phys. Rev. A **26**, 1200 (1982).

[22] E. H. Lieb, Int. J. Quantum. Chem. **24**, 243 (1983).

[23] W. Kohn and J. Sham, Phys. Rev. **140**, A1133 (1965).

[24] J. P. Perdew and S. Kurth, in *A Primer in Density Functional Theory*, edited by C. Fiolhais, F. Nogueira, and M. Marques (Springer, Berlin, 2003), p. 1.

[25] J. P. Perdew and A. Zunger, Phys. Rev. B **23**, 5048 (1981).

[26] D. M. Ceperley and B. J. Alder, Phys. Rev. Lett. **45**, 566 (1980).

[27] S. Kahana, Phys. Rev. **129**, 1622 (1963).

[28] J. P. Carbotte and S. Kahana, Phys. Rev. **139**, A213 (1965).

[29] E. Daniel and S. H. Vosko, Phys. Rev. **120**, 2041 (1960).

[30] A. Salvadori and J. P. Carbotte, Phys. Rev. **188**, 550 (1969).

[31] B. B. J. Hede and J. P. Carbotte, J. Phys. Chem. Solids **33**, 727 (1972).

[32] J. Arponen and E. Pajanne, Ann. Phys. (N.Y.) **121**, 343 (1979).

[33] L. J. Lantto, Phys. Rev. B **36**, 5160 (1987).

[34] E. Boroński and R. M. Nieminen, Phys. Rev. B **34**, 3820 (1986).

[35] R. M. Dreizler and E. K. U. Gross, *Density Functional Theory* (Springer-Verlag, Berlin, 1990).

[36] L. Gilgien, G. Galli, F. Gygi, and R. Car, Phys. Rev. Lett. **72**, 3214 (1994).

[37] M. J. Puska, A. P. Seitsonen, and R. M. Nieminen, Phys. Rev. B **52**, 10947 (1995).

[38] M. Saito and A. Oshiyama, Phys. Rev. B **53**, 7810 (1996).

[39] Z. Tang, M. Hasegawa, T. Chiba, M. Saito, A. Kawasuso, Z. Q. Li, R. T. Fu, T. Akahane, Y. Kawazoe, and S. Yamaguchi, Phys. Rev. Lett. **78**, 2236 (1997).

[40] D. V. Makhov and L. J. Lewis, Phys. Rev. B **71**, 205215 (2005).

[41] M. J. Puska and R. M. Nieminen, J. Phys. F **13**, 333 (1983).

[42] G. Kresse and D. Joubert, Phys. Rev. B **59**, 1758 (1999).

[43] S. Goedecker and K. Maschke, Phys. Rev. B **45**, 1597 (1992).

[44] M. J. Puska, S. Mäkinen, M. Manninen, and R. M. Nieminen, Phys. Rev. B **39**, 7666 (1989).

[45] B. Barbiellini, M. J. Puska, T. Torsti, and R. M. Nieminen, Phys. Rev. B **51**, R7341 (1995).

[46] B. Barbiellini, M. J. Puska, T. Korhonen, A. Harju, T. Torsti, and R. M. Nieminen, Phys Rev. B **53**, 16201 (1996).

[47] J. M. Campillo Robles, E. Ogando, and F. Plazaola, J. Phys.: Condens. Matter **19**, 176222 (2007).

[48] I. R. Epstein and W. N. Lipscomb, J. Chem Phys. **53**, 4418 (1970).

[49] P. Duffy, D. P. Chong, M. E. Casida, and D. R. Salahub, Phys. Rev. A **50**, 4707 (1994).

[50] L. Lam and P. M. Platzman, Phys. Rev. B **9**, 5122 (1974).

[51] P. Eisenberger and P. M. Platzman, Phys. Rev. A **2**, 415 (1970).

[52] R. A. Ferrell, Rev. Mod. Phys. **28**, 308 (1956).

[53] S. Daniuk, G. Kontrym-Sznajd, A. Rubaszek, H. Stachowiak, J. Mayers, P. A. Walters, and R. N. West, J. Phys. F **17**, 1365 (1987).

[54] T. Jarlborg and A. K. Singh, Phys. Rev. B **36**, 4660 (1987).

[55] S. Daniuk, M. Šob, and A. Rubaszek, Phys. Rev. B **43**, 2580 (1991).

[56] M. Šob, in *Proc. of the 8th Annual Int. Symp. on Electronic Structure of Metals and Alloys, Gaussig, Germany*, edited by P. Ziesche (Tech. Universität Dresden, Dresden, 1978), p. 170.

[57] M. Šob, in *Positron annihilation (Proc. 5th Int. Conf. on Positron annihilation, Lake Yamanaka, Japan)*, edited by R. R. Hasiguti and K. Fujiwara (The Japanese Institute of Metals, Sendai, 1979), p. 309.

[58] P. E. Mijnarends and R. M. Singru, Phys. Rev. B **19**, 6038 (1979).

[59] M. Šob, H. Sormann, and J. Kuriplach, Adv. Quantum Chem. **42**, 77 (2003).

[60] M. Alatalo, B. Barbiellini, M. Hakala, H. Kauppinen, T. Korhonen, M. J. Puska, K. Saarinen, P. Hautojärvi, and R. M. Nieminen, Phys. Rev. B **54**, 2397 (1996).

[61] B. Barbiellini, M. Hakala, M. J. Puska, R. M. Nieminen, and A. A. Manuel, Phys. Rev. B **56**, 7136 (1997).

[62] Y. Nagai, T. Honma, Z. Tang, K. Hono, and M. Hasegawa, Phil. Mag. A **82**, 1559 (2002).

[63] S. Ishibashi, Mater. Sci. Forum **445–446**, 401 (2004).

[64] A. Uedono, N. Hattori, H. Naruoka, S. Ishibashi, R. Suzuki, and T. Ohdaira, J. Appl. Phys. **97**, 023532 (2005).

[65] A. Uedono, K. Ikeuchi, T. Otsuka, K. Yamabe, K. Eguchi, M. Takayanagi, S. Ishibashi, T. Ohdaira, M. Muramatsu, and R. Suzuki, J. Appl. Phys. **100**, 034509 (2006).

[66] G. Kresse and J. Furthmüller, Comput. Mat. Sci. **6**, 15 (1996).

[67] G. Kresse and J. Furthmüller, Phys. Rev. B **54**, 11169 (1996).

[68] T. Torsti, V. Lindberg, I. Makkonen, E. Ogando, E. Räsänen, H. Saarikoski, M. J. Puska, and R. M. Nieminen, Ψ_k Newsletter, Highlight of the month, **No. 65**, 105 (October 2004).

[69] M. Heiskanen, T. Torsti, M. J. Puska, and R. M. Nieminen, Phys. Rev. B **63**, 245106 (2001).

[70] P. Valminen, Special Assignment, Helsinki University of Technology, 2002.

[71] *X-Ray Compton Scattering*, edited by M. J. Cooper, P. E. Mijnarends, N. Shiotani, N. Sakai, and A. Bansil (Oxford University Press, Oxford, 2004).

[72] E. D. Isaacs, A. Shukla, P. M. Platzman, D. R. Hamann, B. Barbiellini, and C. A. Tulk, Phys. Rev. Lett. **82**, 600 (1999).

[73] Y. Kubo, Y. Sakurai, Y. Tanaka, T. Nakamura, H. Kawata, and N. Shiotani, J. Phys. Soc. Jpn. **66**, 2777 (1997).

[74] P. Delaney, B. Králik, and S. G. Louie, Phys. Rev. B **58**, 4320 (1998).

[75] Y. Sakurai, Y. Tanaka, A. Bansil, S. Kaprzyk, A. T. Stewart, Y. Nagashima, T. Hyodo, S. Nanao, H. Kawata, and N. Shiotani, Phys. Rev. Lett. **74**, 2252 (1995).

[76] T. Ohata, M. Itou, I. Matsumoto, Y. Sakurai, H. Kawata, N. Shiotani, S. Kaprzyk, P. E. Mijnarends, and A. Bansil, Phys. Rev. B **62**, 16528 (2000).

[77] K. Nygård, M. Hakala, T. Pylkkänen, S. Manninen, T. Buslaps, M. Itou, A. Anderjczuk, Y. Sakurai, M. Odelius, and K. Hämäläinen, J. Chem. Phys. **126**, 154508 (2007).

[78] A. Lietoila, J. F. Gibbons, and T. W. Sigmon, Appl. Phys. Lett. **36**, 765 (1980).

[79] P. M. Fahey, P. B. Griffin, and J. D. Plummer, Rev. Mod. Phys. **61**, 289 (1989).

[80] P. M. Voyles, D. A. Muller, J. L. Grazul, P. H. Citrin, and H.-J. L. Gossmann, Nature **416**, 826 (2002).

[81] P. M. Voyles, D. J. Chadi, P. H. Citrin, D. A. Muller, J. L. Grazul, P. A. Northrup, and H.-J. L. Gossmann, Phys. Rev. Lett. **91**, 125505 (2003).

[82] D. J. Chadi, P. H. Citrin, C. H. Park, D. L. Adler, M. A. Marcus, and H.-J. Gossmann, Phys. Rev. Lett. **79**, 4834 (1997).

[83] K. Saarinen, T. Suski, I. Grzegory, and D. C. Look, Phys. Rev. B **64**, 233201 (2001).

[84] A. F. Wright, J. Appl. Phys. **90**, 1164 (2001).

[85] R. Saniz, B. Barbiellini, and A. Denison, Phys. Rev. B **65**, 245310 (2002).

[86] T. Chiba, Y. Nagai, Z. Tang, T. Akahane, M. Hasegawa, M. Takenaka, and E. Kuramoto, Mater. Sci. Forum **445–446**, 380 (2004).

[87] M. H. Weber, K. G. Lynn, B. Barbiellini, P. A. Sterne, and A. B. Denison, Phys. Rev. B **66**, 041305 (2002).

[88] J. Friedel and M. Peter, Europhys. Lett. **8**, 79 (1989).

[89] A. Somoza, M. P. Petkov, K. G. Lynn, and A. Dupasquier, Phys. Rev. B **65**, 094107 (2002).

[90] R. Ferragut (unpublished).

[91] R. Ferragut, A. Dupasquier, G. Ferro, M. Biasini, and A. Somoza, Mater. Sci. Forum **445–446**, 75 (2004).

[92] R. Ferragut, G. Ferro, and M. Biasini, Mater. Forum **28**, 1022 (2004).

[93] R. Ferragut, A. Dupasquier, M. M. Iglesias, C. E. Macchi, A. Somoza, and I. J. Polmear, Mater. Sci. Forum **519–521**, 309 (2006).

[94] M. Massazza, G. Riontino, D. Lussana, A. Ioazzia, P. Mengucci, G. Barucca, A. Di Cristoforo, R. Ferragut, and R. Doglione, *Magnesium Alloys and their applications* (Wiley-VCH, Weinheim, 2006), p. 466.

[95] E. Boroński, Europhys. Lett. **75**, 475 (2006).